Entanglement effects in defect-free model polymer networks

New Journal of Physics
An Institute of Physics and Deutsche Physikalische Gesellschaft Journal

Entanglement effects in defect-free model polymer networks

Ralf Everaers

Max-Planck-Institut für Polymerforschung, Postfach 3148, D-55021 Mainz, Germany
Institut Curie, Section de recherche, 26 rue d'Ulm, F-75248 Paris Cedex 05, France
Institut für Festkörperforschung, Forschungszentrum Jülich, Postfach 1913, D-52425 Jülich, Germany
E-mail: everaers@mpip-mainz.mpg.de

New Journal of Physics **1** (1999) 12.1–12.54 (http://www.njp.org/)
Received 22 September 1998; online 28 July 1999

Abstract. The influence of topological constraints on the local dynamics in crosslinked polymer melts and their contribution to the elastic properties of rubber elastic systems are long standing problems in statistical mechanics. Polymer networks with diamond lattice connectivity are idealized model systems which isolate the effect of topology conservation from other sources of quenched disorder. By studying their behaviour in molecular dynamics simulations under elongational strain we are able to measure the microscopic deformations as well as the purely entropic shear moduli. In our analysis we make extensive use of the microscopic structural and topological information available in computer simulations and present quantitative tests of the concepts underlying most statistical mechanical models of rubber elasticity.

Contents

1367-2630/99/000012+54$19.50

Overview

Polymer networks [1] are the basic structural element of systems as different as tire rubber and gels and have a wide range of technical and biological applications. While they have been a subject of statistical mechanics for more than sixty years, their rigorous treatment still presents a challenge. Similar to spin glasses [3], the main difficulty is the presence of quenched disorder over which thermodynamic variables need to be averaged. In the case of polymer networks [7, 2], the vulcanization process leads not only to a randomly connected solid but freezes (due to the mutual impenetrability of the polymer backbones) also the topological state of the network. While for a given connectivity the phantom model Hamiltonian for non-interacting polymer chains formally takes a simple quadratic form [4]–[6], treating the topological aspects is much harder for several reasons: (i) Topological constraints do not enter the Hamiltonian as such, but divide phase space into accessible and inaccessible regions characterized by topological invariants from mathematical knot theory [9]; (ii) The common topological invariants can be used to characterize knots formed by individual strands or links between mesh pairs. However, in principle one requires an infinte set of higher order invariants [8]; (iii) All but the most primitive invariants are algebraic [9] so that their statistics cannot be calculated analytically for entangled random walks [87].

So far no rigorous solution of the statistical mechanics of entangled polymer networks exists. Topological theories of rubber elasticity [2, 7, 8], [10]–[18] represent the most fundamental

approach, but encounter serious mathematical difficulties already on the level of pairwise entanglement between meshes. Most theories do, however, omit such a detailed description in favour of a mean-field ansatz where the different parts of the network are thought to move in a deformation-dependent elastic matrix which exerts restoring forces towards some rest positions. The classical theories [1, 19], [20]–[23] assume that such forces only act on the cross-links or junction points, while the tube models [24]–[28] stress the importance of the topological constraints acting along the contour of strands exceeding a minimum 'entanglement length'.

It is the purpose of this paper to quantitatively test the ideas underlying the topological, classical and tube models in computer simulations of idealized model networks with diamond lattice connectivity. Being free of defects, these systems allow us to isolate the effects of topology conservation from those of chemical disorder. In view of the complexity of real networks such a simplification seems adequate and be it only in order to prepare more comprehensive studies. In particular, we address the following questions.

(i) In an attempt to give a more precise meaning to the term 'entanglement', what is the topological degree of linking of the network meshes?

(ii) What is the entanglement contribution to the macroscopic shear modulus?

(iii) In what manner (i.e. classical versus tube model) do entanglements affect the microscopic mean conformations and fluctuations of the networks in the unstrained state?

(iv) How does the confinement change under strain?

(v) Is it possible to calculate the macroscopic restoring forces from the microscopic deformations? (In particular, are there non-classical contributions to the elastic response?)

(vi) Is it possible to predict the network conformations under strain from an analysis of the fluctuations in the unstrained state (i.e. based on the knowledge of the actual strength of the confining potentials)?

(vii) As a complementary question, can one estimate the entanglement contribution to the shear modulus from a simple model for the topological interactions?

(viii) Is it perhaps even possible to *derive* the degree of confinement or the tube model along these lines?

1. Introduction

From a macroscopic point of view, rubber-like materials have very distinct visco- and thermoelastic properties [1, 25]. They reversibly sustain elongations of up to 1000% with small strain elastic moduli which are four or five orders of magnitude smaller than for other solids. Maybe even more unusual are the thermoelastic properties discovered by Gough and Joule in the 19th century: when heated, a piece of rubber under a constant load *contracts*, and, conversely, heat is *released* during stretching. With the advent of statistical mechanics it became clear that the stress induced by a deformation had to be almost exclusively due to a *decrease in entropy*. The microscopic origin of this entropy change remained, however, obscure until the discovery of polymeric molecules and their high degree of conformational flexibility in the 1930s. In a melt of identical chains polymers adopt random coil conformations [29] with mean-square end-to-end distances proportional to their length, $\langle r^2 \rangle \sim N$. A simple statistical mechanical argument, which only takes the connectivity of the chains into account, then suggests that flexible polymers react to forces on their ends as linear, *entropic springs*. The spring constant, $k = \frac{3k_{\mathrm{B}}T}{\langle r^2 \rangle}$,

is proportional to the temperature. Treating a piece of rubber as a random network of non-interacting entropic springs (the phantom model [4]–[6], see figure 1 (a) and section 2.1 for details) qualitatively explains the observed behaviour, including—to a first approximation—the shape of the measured stress–strain curves. Within this model, the only remaining problem is the complicated connectivity of a randomly cross- or end-linked melt of linear precursor chains. A proper treatment of the frozen chemical disorder is essential in order to understand swollen networks [30] and the vulcanization transition [31], but seems uncritical for highly cross-linked networks (i.e. with many cross-links per precursor chain) [6], [32]–[34].

In this paper we are concerned with a different kind of quenched disorder which is not due to the connectivity but another characteristic property of polymers: their mutual impenetrability and the resulting entanglements [1, 2, 7, 8], [10]–[28], [36]–[47]. The classical view of the entanglement problem (see figure 1 and Secs. 2.3 and 2.5 for details), often associated with the name of Flory, is to assume that the main effect is a partial suppression of the junction fluctuations relative to the predictions of the phantom model [19]–[23]. The oldest model of rubber elasticity, the junction affine model [1], is recovered in the limit of immobile junction points, whose instantaneous positions then deform affinely with the sample. The classical theories predict that entanglements only cause a modest increase (typically up to a factor of two compared to the phantom model) of the shear modulus. In particular, $G \sim \rho_{\mathrm{strand}} k_{\mathrm{B}} T = \frac{\rho}{N} k_{\mathrm{B}} T$ is predicted to vanish in the limit of infinitely long network strands.

There are, however, good reasons to suspect that the classical theories overlook important aspects of the physics of an entangled network which influence (i) the fluctuations of the network strands *between* the junction points and (ii) the absolute value of the shear modulus. The evidence comes from the study of non-cross-linked polymer melts, which show extremely slow relaxation as soon as the chain length N exceeds a phenomenological 'entanglement length', N_{e}. A simple and very successful explanation of these effects is provided by the tube model of Edwards [24] and the reptation theory [48] of de Gennes. The idea is that the presence of the other polymers restricts a chain to fairly small fluctuations inside a tube-like region with a cross-section of the order of $\langle r^2 \rangle (N_{\mathrm{e}})$ along its coarse grained contour (figure 2 (a)). A polymer can loose the memory of its initial conformation only by a one-dimensional, curvilinear diffusion along and finally out of its original tube ('reptation'). The geometrical constraint is relatively easy to handle analytically and on a mean-field level the tube model provides a unified view on networks and entangled polymer melts [25]–[28]. In particular, one expects that under shear deformations each chain segment of length N_{e} behaves as an independent entropic spring, leading to a chain length independent (plateau) modulus $G \sim \frac{\rho}{N_{\mathrm{e}}} k_{\mathrm{B}} T$. In a melt, this shear stress relaxes over a time $\tau_{max} \sim N^3$ by reptation, while in a network the chemical cross-links suppress this mechanism. Thus, in contrast to the classical models, the tube models predict a finite shear modulus in the limit $N \to \infty$.

Both the constrained junction and the tube model are based on the idea that partially constrained fluctuations lead to non-trivial microscopic deformations and contribute to the elastic response. The close relation between the two approaches (of which the tube model is in fact the older one, even though the constrained junction models completed the classical theories) is emphasized in two recent models by Rubinstein and Panyukov [41] and the present author [42]. For quantitative comparisons we use in this paper the constrained mode model (CMM) [42] (section 2.3) which is particularly suited for the analysis of simulation data. The CMM is based on the assumption that deformation dependent linear forces couple to (approximate) *eigenmodes* of the phantom network. On the one hand (figure 1), we use Einstein modes describing the

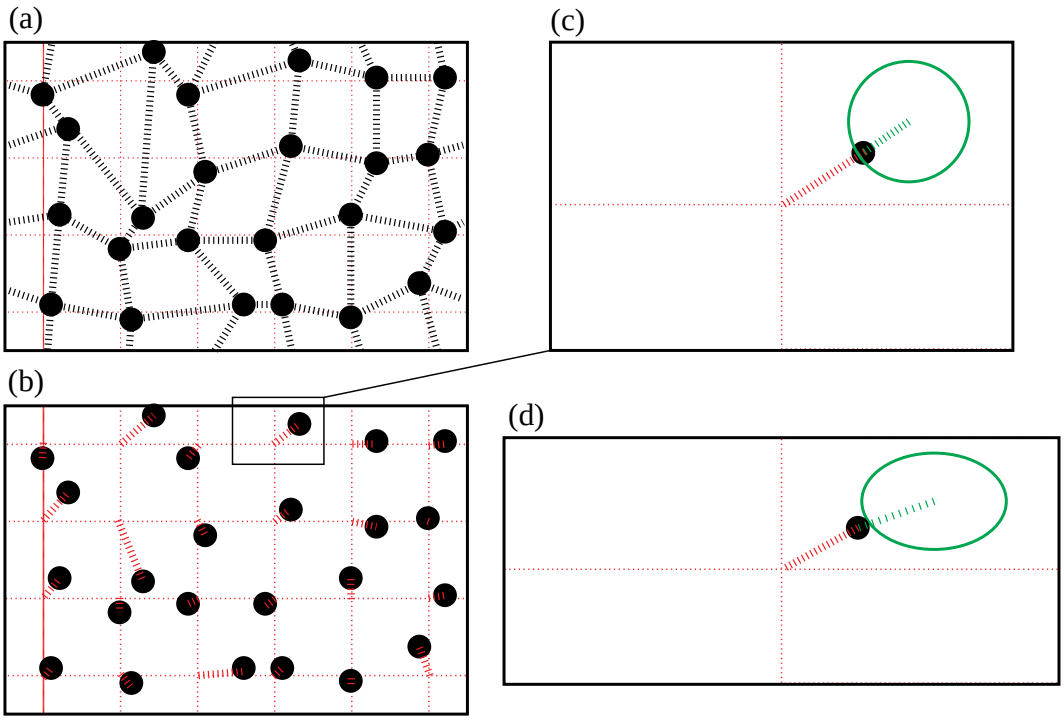

Figure 1. The classical models of rubber elasticity. (a) The phantom model: the network strands are replaced by linear, non-interacting, entropic springs. The grid marks the equilibrium positions for the drawn phantom network with square lattice connectivity. When the system is deformed, the equilibrium positions move affinely with the macroscopic strain. The fluctuations are deformation independent and do *not* contribute to the elastic response. (b) The same system using the Einstein approximation of independently fluctuating cross-links. (c) The constrained junction model: entanglements restrict the motion of the cross-links to small cavities which are positioned randomly around the equilibrium positions. The position of the minima and the strength of the constraining potentials have to be chosen in such a way that snapshots of the system have the same statistics as in the phantom case. (d) Microscopic versus macroscopic deformations: the centres of the cavities move as the phantom model equilibrium positions affinely with the macroscopic deformation of the network. As a consequence, partially constrained modes become anisotropic and contribute to the elastic response. The deformation dependence of the constraining potentials leads in general to non-trivial microscopic deformations. The limit of infinitely strong confining potential corresponds to the junction affine model, the oldest theory of rubber elasticity.

motion of the junction points. On the other hand (figure 2, for details see section 2.6), we analyse the motion of the network strands in terms of single chain Rouse modes for immobile endpoints. In this manner one can directly separate the classical and non-classical contributions to the elastic response and recover the constrained junction and the tube model as limiting cases. Even more important from a practical point of view is the possibility to obtain within one

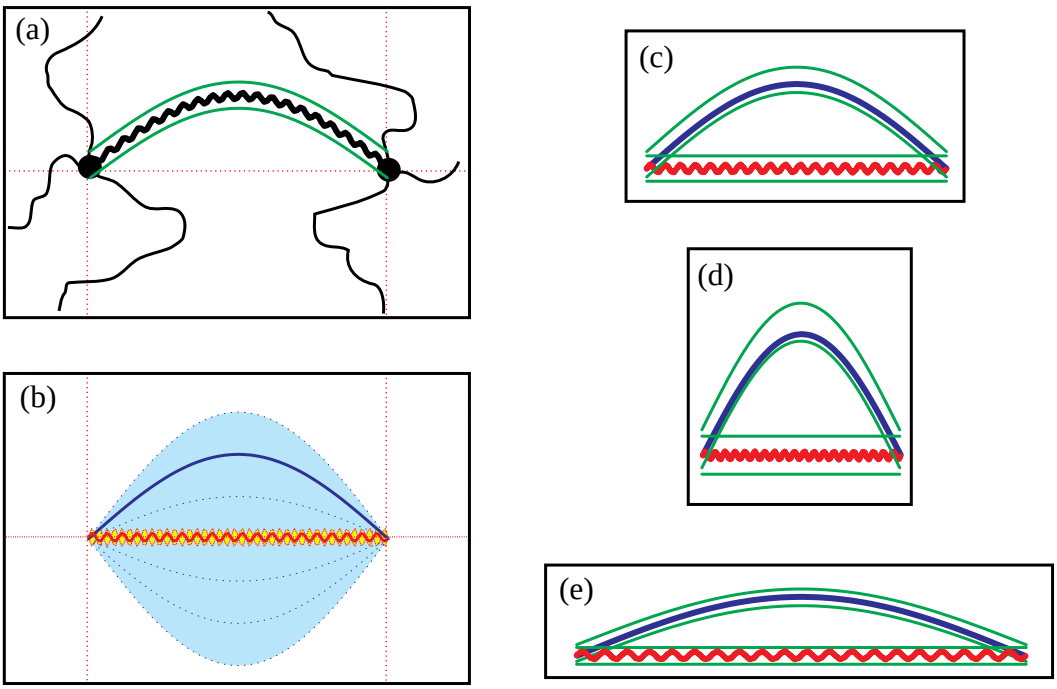

Figure 2. The tube model: (a) Entanglements confine a network strand with $N_{\rm strand} > N_{\rm e}$ to a tube-like region around its coarse-grained contour. (b) The conformation of the strand can be written as a superposition of independent Rouse modes for fixed endpoints. The dotted lines and shaded areas indicate the larger range of thermal excitation of long (blue) than short (red) wavelength modes. (c) The constrained mode model: entanglements are modeled as acting independently on each Rouse mode. Short wave length modes are not affected by the tube-like constraint, while long wave length modes are restricted to fluctuations around a non-vanishing mean value which are much smaller than their thermal fluctuations. The formal treatment is identical for the Rouse and the Einstein modes in figure 1 (d) (e) In particular, as the tube deforms with the sample, partially constrained modes become anisotropic and contribute to the restoring forces. The deformation-dependence of the constraining potentials leads to weaker than affine microscopic deformations.

transparent formalism meaningful results for systems with arbitrary strand lengths N, ranging from networks with $N \ll N_{\rm e}$, which should be well described by classical rubber elasticity, to entanglement dominated systems with $N \gg N_{\rm e}$.

Topological theories of rubber elasticity have an even longer history than the tube model and represent a more fundamental approach, from which it might be possible to *derive* the constrained fluctuation models (including estimates for the parameters characterizing the *strength* of the confinement such as the entanglement length $N_{\rm e}$). Thirty years ago, Prager and Frisch [10], Edwards [7], and later Vologodskii *et al* [37, 38] argued that forces can be transmitted between two ring polymers which are not chemically connected but topologically linked. Edwards [2, 7, 8] suggested calculating the elastic response from quenched averages in which topological invariants characterizing the degree of linking of all mesh pairs are conserved. This represents already

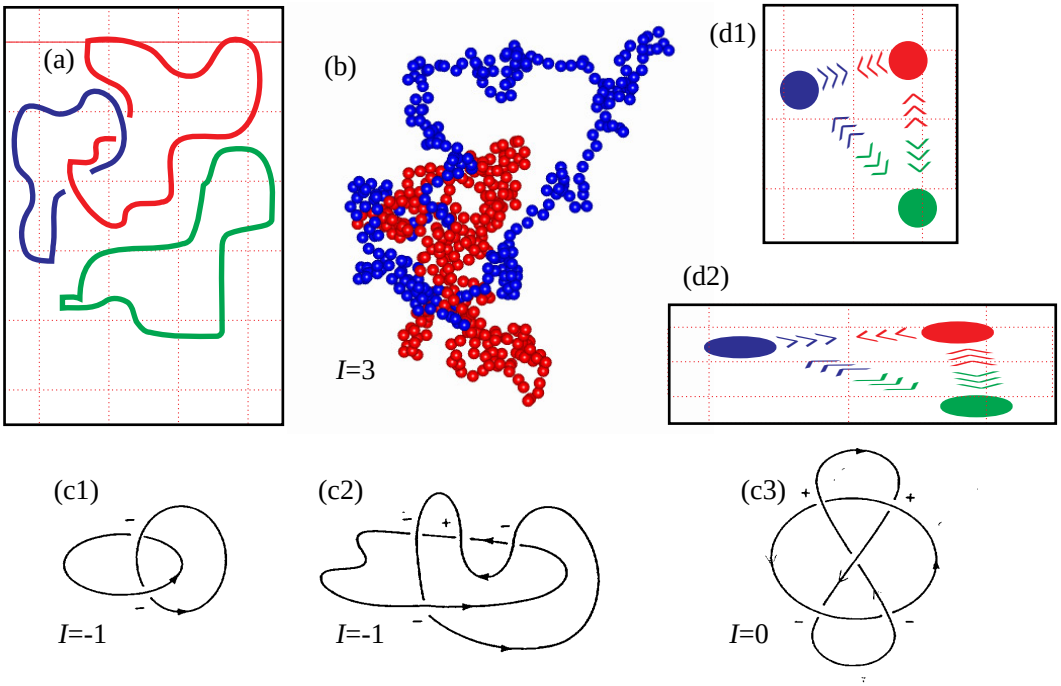

Figure 3. The topological models of rubber elasticity: (a) The topological state of a network is a conserved quantity. Often one considers only the pairwise entanglement of the network meshes, even though in principle an infinite set of higher order interactions should be taken into account as well. (b) Example of two multiply entangled meshes in random IPDN with $N = 44$. (c) The Gauss linking number, I, is a simple topological invariant. It can either be calculated from a double integral over the ring contours (Eq. 19) or by a method where all crossing points of the two curves in a projection are indexed by $\pm 1/2$ [35]. The sign depends on the direction into which the tangent vector of the upper curve has to be rotated in order to coincide with the one of the bridged curve. The linking number I is defined as the sum of the indices and is *invariant* under distorsions of the rings (c2). There are examples of linked curves with $I = 0$, so that the classification is not completely reliable (c3). (d1) Approximation of the topological pair interaction by an entropic attraction (respectively repulsion) between the centres of mass (CM) of topologically linked (respectively non-linked) meshes. The origin of this effect lies in the reduction of the number of accessible states for two linked ring polymers with increasing CM distance. The precise form of the effective potential follows from the CM distance dependent linking probability. (d2) In a simple application of these ideas to networks one can estimate a link contribution to the shear modulus from the assumption that the mesh centres move affinely with the macroscopic deformation and that the effective topological interaction is deformation independent.

a drastic simplification as in principle an infinite set of topological invariants is required to characterize the state of a network [8]. So far even the binary entanglement problem has proven too complex for a rigorous solution [2],[12]–[18], but the underlying physics is preserved in the

simple model by Graessley and Pearson [11] (figure 3, for details see section 2.7). In particular, its predictions for the entanglement contribution to the shear modulus can be tested quantitatively in computer simulations [49]. Here we will provide more details, but note already at this point that even though the results are encouraging for the present systems, a different approach will be required in order to actually derive the tube model [15, 50].

Not least due to their technical importance, rheological studies on polymer networks have been an area of active research for more than half a century. It is therefore quite remarkable that there is no definite experimental answer to the question, if and how much entanglement effects contribute to the elasticity of such systems [51]–[64]. Most of the experimental data seems to be well described by the classical models. The constrained junction models [19]–[23] in particular have been shown to provide an excellent parametrization of the stress–strain curves [58, 63]. However, often the data can be described equally well by expressions derived from tube models or variants thereof [55]–[57], [65]. In fact, it is even possible to derive formally identical stress–strain relations from models which have completely opposite views on the effect of topological constraints [66]. The distinction between the various theoretical approaches can therefore not be made on the basis of the *shape* of stress–strain curves alone.

A critical test requires a comparison of the absolute values of measured and predicted moduli or, less specifically, the extrapolation of the measured moduli to the limit of vanishing cross-link density where the classical contribution to the modulus vanishes. Such investigations have indicated from early on that the classical theories underestimate the modulus [51, 52]. However, it is quite difficult to prepare model networks with a well defined density of chains in the elastically active cluster, ρ_{strand}. This holds in particular in the limit $N \gg N_{\mathrm{e}}$. A randomly cross-linked melt of linear polymers has a highly irregular connectivity. Typical defects are polydispersity, dangling ends and clusters, and self-loops. Efforts have therefore concentrated on the preparation of model networks by end-linking. While some groups have claimed to have prepared nearly ideal networks [58]–[60], others have shown that this state is impossible to reach for large strand lengths [53, 54]. The reason for the imperfect network structures are the exponentially long times required towards the end of the synthesis to pair the remaining unsaturated chain ends [67]. Patel *et al* [62] have used swelling experiments in order to restrict their analysis to those of their samples with the highest degree of conversion. Their results indicate indeed a non-vanishing shear modulus in the limit of infinite strand length.

A more detailed test and comparison of the theoretical models requires access to microscopic information not available in rheological experiments. Much insight can be gained experimentally in small-angle neutron-scattering experiments [68]–[70]. By these techniques it is, for example, possible to detect and quantify the tube-like confinement of the chain motion in polymer melts and networks, to investigate the effect of shear deformations on the tube, and to compare the results to theoretical predictions.

An alternative, which we shall pursue in this paper, are large scale computer simulations of suitably coarse-grained polymer models [71]. Bearing in mind the limitations in the accessible time and length scales, they offer a couple of advantages compared to experiments: a greater freedom in and control over the formation of the networks, a more direct access to the microscopic structure and dynamics (e.g. the restriction of the data analysis to elastically active chains), and the realization of Gedankenexperiments such as the comparison of otherwise identical systems with and without topology conservation. Simulations of coarse-grained models provided the first direct evidence for the tube/reptation model in polymer melts [72, 73], gave inside into the kinetics of end-linking [67, 74] and the structure of the resulting networks [75],

demonstrated the importance of topological constraints for the relaxation of cross- and end-linked networks [75, 76], and showed quantitatively the failing of the predictions of the classical models for the elastic modulus [77, 78]. An important point is the good agreement between experimental and simulation results for the chain mobilities and the elastic properties when mapped onto universal curves [71] as it confirms that the simulation methods we employ are capable of covering the experimentally relevant time and length scales.

In this paper we give a detailed account of molecular dynamics simulations of model polymer networks with diamond lattice connectivity [49], [78]–[80]. While such systems cannot be prepared experimentally, they offer some considerable advantages in a numerical study addressing fundamental aspects of the entanglement problem. First, since there are no 'chemical' defects, diamond networks isolate the effects of topology conservation from those of other types of quenched disorder. Second, in the absence of dangling ends and clusters, the longest relaxation times in these systems are the Rouse times of single network strands.

The individual diamond networks are spanned across the simulation volume via periodic boundary conditions. In the spirit of the Flory-Rehner four-chain model [81] we have chosen an average distance between connected cross-links equal to the root mean square end–to–end distance of the corresponding chains in a melt. The density of a single diamond net decreases with the strand length. To reach melt density we place several of these structures in the simulation box and work with inter-penetrating diamond networks (IPDN). As a consequence, cross-links which are nearest neighbours in space will usually belong to different diamond nets and will not be connected by network strands. The same holds true in experimental systems, which can be said to be *locally* inter-penetrating [20]. The regular connectivity in our systems affects only length scales beyond the size of the network strands.

We follow two distinct strategies to isolate the entanglement effects. One is to calculate quenched averages for otherwise identical systems with different topology. In our simulations of random and of regular IPDN we employ interaction potentials which ensure the mutual impenetrability of the chains, thereby preserving the topological state from the end of the preparation process. The second strategy is to calculate annealed averages over different topologies. This can either be achieved trivially by simulating non-interacting phantom chains or by using interaction potentials that allow chains to cut through each other but nevertheless preserve the monomer packing of the melt [76]. The structure of the chains is almost identical for all systems and by comparing their behaviour we can directly access the effects of the topological constraints. The preparation of our most important systems, the random IPDN, is illustrated in video-sequence 1.

By investigating strained samples we obtained the first reliable measurements of the elastic properties of model polymer networks in a computer simulation [78, 79]. Since we also have complete access to the microscopic structure and dynamics in both, the strained and the unstrained state, we are in a unique position to test statistical mechanical theories of rubber elasticity which are based on a well-defined microscopic picture. While the quantitative analysis will exclusively be concerned with moderate deformations of the order of 50%, some qualitative insight into the importance of entanglements can already be gained by analysing the microscopic stress distribution in strongly stretched random IPDNs as in figure 4 and the video sequence 2. Chemical bonds which carry high tensions are shown with a larger diameter and marked in red. A large part of the tension is localized on topologically shortest paths through the system. In particular, these paths are composed of strands as well as meshes with physical entanglements propagating the tension *in the same manner as chemical cross-links*. This stress localization in random IPDNs is

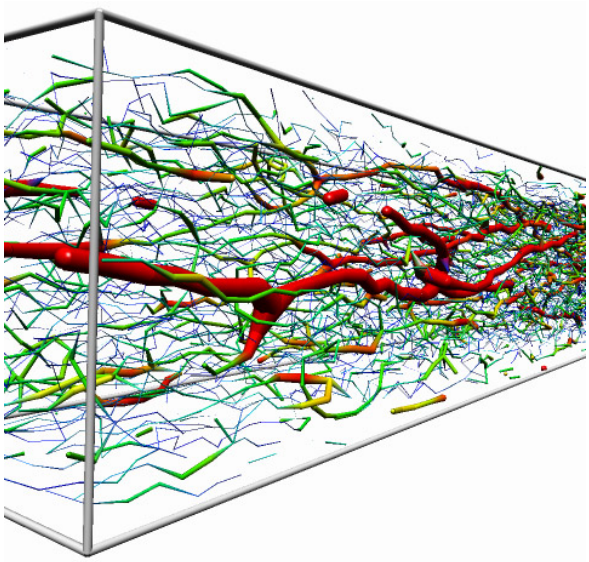

Figure 4. Conformation of highly strained random IPDN ($\lambda = 3.2$) [80]. In the non-linear regime a large part of the stress is localized on topologically shortest paths through the system (bonds carrying high tensions are marked by thick radii and in red). Note that physical entanglements propagate the tension in the same manner as chemical cross-links. The apparant interruption of the chains is due to the representation in periodic boundary conditions.

completely unexpected from the point of view of the classical theory, since all network strands are equivalent. The more artificial regularly IPDN mimic a situation where this equivalence is preserved for a conserved topology. When these networks are stretched, all strands contribute equally to the elastic response. Tensions are homogeneous throughout the whole system, and all strands are stretched to their full contour length at the maximal elongation.

In order to keep the paper in spite of its considerable length accessible to the reader, we have tried to structure the presented material as much as possible. For a first reading, it should be possible to pass directly to the discussion in section 5. The theoretical background is presented in section 2, a description of the simulation techniques and the detailed presentation of the simulation results can be found in sections 3 and 4 respectively. Two key results of this study have already been published in short notes: the direct proof that the classical explanation of rubber elasticity which only considers the elongation of the network strands cannot account for the observed moduli [78] and the interpretation of the topology contribution to the elastic modulus in terms of mesh entanglements [49]. The graphical illustrations of the preparation of random IPDN and their behaviour under large strain (including a visualization of the propagation of internal stresses by entanglements) were first published in [80]. Some preliminary results have recently been presented at the 11th Max-Born conference [82].

2. Theory

Most current models of rubber elasticity are based on the phantom model [4]–[6] (section 2.1) combined with the idea that entanglements between the polymer chains reduce the fluctuations [1], [25]–[28]. Being deformation dependent, the effective constraints then contribute to the elastic properties of the network. In section 2.3 we discuss these effects in the framework of the constrained mode model (CMM) [42]. The results are then used in sections 2.5 and 2.6 to recover the classical theories of rubber elasticity and the tube model. Finally, we present in section 2.7 the simple topological model of Graessley and Pearson [11]. Secs. 2.2 and 2.4 discuss phantom diamond networks and systems with a quenched regular topology.

2.1. The phantom model

The Hamiltonian of the phantom model [4]–[6] is given by $\mathcal{H}_{\rm ph} = \frac{k}{2}\sum_{\langle i,j<i\rangle} r_{ij}^2$, where $\langle i,j<i\rangle$ denotes a pair of nodes which are connected by a polymer chain acting as an entropic spring of strength $k = \frac{3k_{\rm B}T}{\langle r^2\rangle}$ and $\vec{r}_{ij}(t) = \vec{r}_i(t) - \vec{r}_j(t)$ the distance between them. The problem is most conveniently studied using periodic boundary conditions, which span the network over a fixed volume [2].

Due to the linearity of the springs the problem separates in Cartesian co-ordinates x, y, z. Furthermore, a conformation of a network of harmonic springs can be analysed in terms of either the bead positions $\vec{r}_i(t)$ or the deviations $\vec{u}_i(t)$ of the nodes from their equilibrium positions $\vec{R}_i$. The latter are characterized by a force equilibrium $\sum_j \vec{R}_{ij} \equiv 0$, where j indexes all nodes which are connected with node i. In this representation, the Hamiltonian separates into two independent contributions from the equilibrium extensions of the springs and the fluctuations, which can be written as a sum over independent normal modes or phonons $\vec{u}_p$ [83, 84]:

$$\mathcal{H}_{\rm ph} = \frac{k}{2}\sum_{\langle i,j<i\rangle} \vec{R}_{ij}^2 + \frac{k_p}{2}\sum_p \vec{u}_p^2 \tag{1}$$

If a sample is deformed, the equilibrium positions of the junction points change affinely. The fluctuations, on the other hand, depend only on the connectivity but not on size and shape of the network. The shear modulus of the phantom model can therefore be calculated without having to integrate out the dynamic eigenmodes of the network. Structural averages, on the other hand, do depend on the fluctuations. Consider, for example, the mean-square extension $\vec{R}_{ij}^2 + [\vec{u}_{ij}^2]$ of a network strand.† It follows from the equipartition theorem that the total thermal energy in the fluctuations, $U_{\rm fluc}$, is given by $\frac{3}{2}k_{\rm B}T$ times the number of modes and therefore $U_{\rm fluc} = \frac{3}{2}k_{\rm B}TN_{\rm nodes} = \frac{2}{f}\frac{3}{2}k_{\rm B}TN_{\rm strands}$, where $N_{\rm nodes}$ and $N_{\rm strands}$ are the number of junction points and network strands, which are related by $N_{\rm strands} = \frac{f}{2}N_{\rm nodes}$ in an f-functional network. Equating the thermal energy per strand to $\frac{k}{2}\left\langle \vec{u}_{ij}^2\right\rangle$, one obtains [6, 42, 85]

$$\langle u_{ij}^2\rangle = \frac{2}{f}\left\langle r^2\right\rangle \quad . \tag{2}$$

† We use $[\ldots]$ to denote time and $\langle\ldots\rangle$ to denote ensemble averages.

In this paper we always consider uni-axial elongations

$$\overleftrightarrow{\lambda} = \begin{pmatrix} \lambda & & \\ & 1/\sqrt{\lambda} & \\ & & 1/\sqrt{\lambda} \end{pmatrix} \tag{3}$$

This volume-conserving deformation ($\det(\overleftrightarrow{\lambda}) = 1$) is the standard choice [1] for rubber-like materials, since they can be considered to be incompressible with a Poisson ratio of $\frac{1}{2}$.

The shear modulus of the phantom model is given by

$$G_{\rm ph} = \frac{1}{3}\frac{1}{V}\frac{d^2 F_{\rm ph}}{d\,\lambda^2}\bigg|_{\lambda=1} = \frac{\langle R^2_{\rm strand}\rangle}{\langle r^2\rangle}\,\rho_{\rm strand}\,k_{\rm B}T \tag{4}$$

where $\langle R^2_{\rm strand}\rangle = \langle R^2_{ij}\rangle$ denotes the expectation value of the square of the mean extension of the network strands. The deformation (3) induces a normal stress $\sigma_T = \left\langle \sigma_{xx} - \frac{1}{2}(\sigma_{yy}+\sigma_{zz})\right\rangle = \frac{\lambda}{V}\frac{{\rm d}F}{{\rm d}\lambda}$, where the $\sigma_{\alpha\alpha}$ are the diagonal elements of the microscopic stress tensor, which can be written in the form

$$\begin{aligned}\langle\sigma_T\rangle \;=\; & \sum_{\langle i,j<i\rangle} k\left(X^2_{ij}(\lambda) - \frac{1}{2}\left(Y^2_{ij}(\lambda)+Z^2_{ij}(\lambda)\right)\right) \\ & + \sum_p k_p \left\langle u^2_{px}(\lambda) - \frac{1}{2}\left(u^2_{py}(\lambda)+u^2_{pz}(\lambda)\right)\right\rangle \quad .\end{aligned} \tag{5}$$

Equation (5) is the proper generalization of the usual Doi–Edwards [25] expression for the stress tensor. In the case of the phantom model the second term is deformation independent and vanishes for networks with cubic symmetry. In the long-time limit after a step strain, equation (3), the normal stress converges to

$$\langle\sigma_T\rangle\,(t\to\infty) = (\lambda^2 - \frac{1}{\lambda})G \quad . \tag{6}$$

2.2. Phantom diamond networks

In this paper we study polymer networks with diamond lattice connectivity. As phantom networks they show very large fluctuations (see for example video 6). In spite of the apparent irregularity of individual network conformations, the *average* cross-link positions form a crystal lattice given by the connectivity [4]. Each strand has the same, non-zero mean extension $\left|\vec{R}_1\right|$ equal to the bond length the lattice. This length is in principle arbitrary. In our simulations we have chosen $\left|\vec{R}_1\right| = \sqrt{\langle r^2\rangle}$. The subscript indicates the extension ratio $\lambda = 1$. The distribution of the *mean* strand end-to-end distances is therefore given by $p^{\rm mean}_{\rm strand}(x) = \frac{1}{2}\left(\delta(x-X_1)+\delta(x+X_1)\right)$ with $X_1 = \frac{1}{\sqrt{3}}\left|\vec{R}_1\right|$. †

† The problem of calculating $\langle R^2_{\rm strand}\rangle$ for a randomly cross-linked network was solved by Flory [6]. He noted that the ensemble average of the strand conformations is the same as in a melt, only that for a network it is the result of a convolution of the distribution of *mean* strand extensions $\vec{R}_{ij}$ with fluctuations of the strands around their mean extensions $\vec{u}_{ij}$. Using equation (2) this leaves $\langle R^2_{\rm strand}\rangle = (1-f/2)\,\langle r^2\rangle$ for a randomly cross-linked network.

As shown in the previous section, in a diamond phantom network with four-functional cross-links the strand extensions fluctuate around their mean values by an amount of $\Delta^2 = \frac{1}{2}\langle r^2\rangle$ [6, 85]. For our particular choice of the lattice constant we expect for the vector $\vec{\Delta}_1$ of fluctuation widths in the three spatial dimensions $\left|\vec{\Delta}_1\right|^2 = \frac{1}{2}|\vec{R}_1|^2$. The strand end-to-end distance distribution at any particular instant in time is given by the convolution of $p^{\rm mean}_{\rm strand}(x)$ with the normally distributed fluctuations, [6] yielding a superposition of two symmetric Gaussian peaks of width $\Delta_{1x} = \frac{1}{\sqrt{3}}\left|\vec{\Delta}_1\right|$ around $\pm X_1$:

$$p_{\rm strand}(x) = \frac{1}{2}\frac{1}{\sqrt{2\pi}\Delta_{\lambda x}} \left(\exp(-\frac{(x-X_\lambda)^2}{2\left(\Delta^x_\lambda\right)^2}) + \exp(-\frac{(x+X_\lambda)^2}{2\left(\Delta^x_\lambda\right)^2})\right) \tag{7}$$

with $p(x,y,z) = p(x)p(y)p(z)$, $\vec{R}_\lambda = \overleftrightarrow{\lambda}\ \vec{R}_1$, and $\vec{\Delta}_\lambda = \vec{\Delta}_1$. The shear modulus of our phantom diamond networks is thus given by

$$G_{\rm ph} = \rho_{\rm strand} k_{\rm B} T. \tag{8}$$

2.3. The constrained mode model

The phantom model completely neglects entanglements between network strands due to their mutual impenetrability. The topological constraints strongly reduce the fluctuations, an effect which is often visualized using the image of a tube around the coarse grained contour of a long chain to which its fluctuations are confined. A simple way to account for the confinement of the strands of a polymer network is provided by the constrained mode model (CMM) [42]. Deformation-dependent constraints are modelled as linear forces which act independently on the eigenmodes of the phantom model:

$$\mathcal{H}_{\rm constr} = \sum_p \frac{1}{2}(\vec{u}_p - \vec{v}_p(\lambda))^t\ \overleftrightarrow{l}_p\ (\lambda)\ (\vec{u}_p - \vec{v}_p(\lambda)) \tag{9}$$

The constraint forces vanish at randomly chosen excitations $\vec{u}_p = \vec{v}_p(\lambda)$. The usual restoring forces for a free mode, on the other hand, vanish at $\vec{u}_p = 0$. Both forces are linear with spring constants $\overleftrightarrow{l}_p\ (\lambda)$ and k_p. As a consequence, the *time average* of the Cartesian component α of a *particular mode* is given by fluctuations around non-zero equilibrium values $[u_{p\alpha}] = U_{p\alpha}(\lambda) = \frac{v_{p\alpha}(\lambda)}{k_p/l_{p\alpha\alpha}(\lambda)+1}$ with a reduced amplitude $[\delta u^2_{p\alpha}] \equiv [(u_{p\alpha} - U_{p\alpha}(\lambda))^2] = \frac{k_{\rm B}T}{k_p + l_{p\alpha\alpha}(\lambda)}$.

For randomly quenched topologies the *ensemble average over many equivalent modes* remains unchanged compared to the phantom model. This can be used to express the expectation values in the unstrained state in terms of a single parameter γ_p, which measures how strongly the fluctuations of the pth mode are confined: $\langle u^2_{p\alpha}\rangle = \langle U^2_{p\alpha}\rangle + \langle \delta u^2_{p\alpha}\rangle = \gamma_p \frac{k_{\rm B}T}{k_p} + (1-\gamma_p)\frac{k_{\rm B}T}{k_p}$ with $\gamma_p = \frac{l_p(\lambda=1)}{k_p + l_p(\lambda=1)}$ and $\langle v^2_{p\alpha}\rangle(\lambda=1) = \gamma_p^{-1}\frac{k_{\rm B}T}{k_p}$. The extreme cases are $\gamma_p = 0$ and $\gamma_p = 1$ corresponding to completely free and completely frozen fluctuations respectively.

With the choice [42] $\vec{v}_p(\lambda) = \overleftrightarrow{\lambda}\,\vec{v}_p$ and $\overleftrightarrow{l}_p\,(\lambda) = \left(\overleftrightarrow{\lambda}\right)^{-2}\overleftrightarrow{l}_p$ of affinely moving and deforming constraints the model is now completely specified and some general conclusions can be drawn with respect to the microscopic deformations. The mean excitations,

$$\frac{U_{p\alpha}(\lambda)}{U_{p\alpha}(1)} = \frac{\lambda_{\alpha\alpha}}{(1-\gamma_p)\lambda_{\alpha\alpha}^2 + \gamma_p} \quad , \tag{10}$$

of partially frozen modes deform *sub*-affinely. Only in the limit $\gamma_p \to 1$ one finds $U_p(\lambda) = \lambda U_p(1)$. A similar result holds for the width of the fluctuations:

$$\frac{\langle \delta u_{p\alpha}^2(\lambda)\rangle}{\langle \delta u_{p\alpha}^2(1)\rangle} = \frac{\lambda_{\alpha\alpha}^2}{(1-\gamma)\lambda_{\alpha\alpha}^2 + \gamma} \quad . \tag{11}$$

While the fluctuations are deformation-independent for unconstrained modes, their width increases sub-affinely for $0 < \gamma < 1$. For completely frozen modes with $\gamma \equiv 1$, $\langle \delta u_{p\alpha}^2(\lambda)\rangle \equiv 0$ independent of λ. Not surprisingly, the predictions concerning the elastic properties are also modified compared to the phantom model. First, the confined fluctuations contribute to the small-strain shear modulus:

$$G_{\rm cm} = G_{\rm ph} + \frac{k_{\rm B}T}{V}\sum_p \gamma_p^2 \quad . \tag{12}$$

Second, they produce corrections to the ideal stress–strain behaviour equation (6), which is recovered only in the two limiting cases of $\gamma = 0$ and $\gamma = 1$. When plotted in the usual Mooney–Rivlin form [42], the corrections qualitatively resemble those observed in experiments, which is encouraging but certainly no proof for the correctness of the ansatz.

An interesting point for the data analysis is the continued validity [42] of equation (5) within the CMM (or any other model with affinely deforming constraints) even for partially confined modes. While the true and the entropic normal tensions can therefore be directly compared, this is not the case for the elastic free energy, which is partially stored in the constraints. The time evolution and confinement of the different modes is best characterized by the ensemble average of their auto-correlation function $c_p(t) = \langle \vec{u}_p(t)\cdot\vec{u}_p(0)\rangle$. The quantities discussed in the CMM are related to this function by: $\langle u_p^2\rangle = c_p(0)$, $\langle U_p^2\rangle = \lim_{t\to\infty} c_p(t)$, and $\langle \delta u_p^2\rangle = \lim_{t\to\infty}(c_p(0) - c_p(t))$. The auto-correlation functions can also be used for a heuristic generalization of equation (12) to a time-dependent shear relaxation modulus

$$G_{\rm cm}(t) = G_{\rm ph} + \frac{k_{\rm B}T}{V}\sum_p \left(\frac{\langle \vec{u}_p(t)\cdot\vec{u}_p(0)\rangle}{\langle \vec{u}_p^2\rangle}\right)^2 \quad . \tag{13}$$

Equation (13) reduces to the Rouse-model result [25] $G_{\rm Rouse}(t) = G_{\rm ph} + \frac{k_{\rm B}T}{V}\sum_p {\rm e}^{-2t/\tau_p}$ for $\gamma = 0$ and should decay to the asymptotic value (12) on similar time scales as the true shear relaxation modulus. Equation (13) is slightly different from the expression employed by Duering *et al* [72, 75, 77]. For a discussion of this point see [42].

2.4. Systems with quenched regular topology

A particular situation arises in systems with a conserved *regular* topology such as our regular IPDN. In this case, the fluctuations $\vec{\delta u}_p$ are reduced compared to the phantom model but, due to symmetry, for each mode centred around zero. For the same reason, the time average for each individual mode is identical to the ensemble average over all equivalent modes. However, the latter now differs from the phantom network value. Within the above model, $\vec{v}_p(\lambda) = \vec{U}_p(\lambda) = 0$ and $\langle \delta u_{p\alpha}^2 \rangle = (1 - \gamma_{p\alpha}) \langle u_{p\alpha}^2 \rangle_{\rm ph}$, where γ is defined as before. The deformation dependence is now exclusively described by equation (11). Quite interestingly, there is a contribution to the shear modulus of the form $G_{\rm cm} = G_{\rm ph} + \frac{k_{\rm B}T}{V} \sum_p \gamma_p (1 - \gamma_p)$ even though the mode autocorrelation functions decay to zero. In contrast to the random case, a completely confined mode has a (deformation independent) zero excitation and does therefore not contribute to the shear modulus. For asymmetric confinement, $\gamma_{p\|} \neq \gamma_{p\perp}$, there is a non-vanishing normal stress at zero strain and it is no longer possible to define a simple shear modulus.

2.5. Classical rubber elasticity: the constrained junction models

The classical theories of rubber elasticity [1], [4]–[6], [19]–[23] date back more than half a century and can qualitatively explain many aspects of the physics of rubber elasticity. They are based on the assumption that the elastic response of rubber has its sole origin in the elongation of the network strands. In this view the main effect of entanglements is a partial suppression of the junction fluctuations [19]–[23]. The latter are usually treated as independent, i.e. using the Einstein model for phonons. The parameter γ_p corresponds to $\gamma = \frac{\kappa}{\kappa+1}$ in Flory's first paper on constrained junction models [20].

Consider a particular junction point i of an f-functional network. If one assumes that its topological neighbours are fixed at their equilibrium positions $\vec{R}_j$, a displacement $u_{i\alpha}$ of node i in one spatial direction α requires an energy $\frac{fk}{2} u_{i\alpha}^2$. Treating these displacements as independent eigenmodes ('Einstein modes') with spring constant $k_p = fk$, one can use the equipartition theorem to obtain $\langle u_{i\alpha}^2 \rangle = \frac{k_{\rm B}T}{fk}$. As a consistency check, we note that this result implies that the extension of a particular network strand should undergo thermal fluctuations of a width $\langle |\vec{u}_{ij}|^2 \rangle = 2 \langle |\vec{u}_i|^2 \rangle = 2 \times 3 \frac{k_{\rm B}T}{fk} = \frac{2}{f} \langle r^2 \rangle$ in agreement with equation (2). In fact, using this argument one can simplify the data analysis and follow the fluctuations of the extensions of the network strands instead of the cross-link motion.

The strength of the confinement can be estimated using arguments from the tube model. For network strands whose length exceed the melt entanglement length $N_{\rm e}$ the fluctuations of the junction points are restricted to the tube diameter $\langle r^2 \rangle (N_{\rm e})$. In this case one finds $N_{\rm e} \sim \langle \delta u_{p\alpha}^2 \rangle = (1 - \gamma_p) \langle u_{p\alpha}^2 \rangle \sim (1 - \gamma_p) N$ or $\gamma = 1 - \frac{N_{\rm e}}{N}$. Contrary to what one might expect, the constrained junction model predicts deformations of the mean strand extensions, which for $\lambda > \sqrt{N/N_{\rm e}}$ are much weaker than affine. This was already noted by Flory, who did, however, not make the connection to the tube model.

In the limit of infinitely long chains, $N \to \infty$, one recovers the predictions of the oldest model of rubber elasticity, the junction affine model. Using the result that there are $\frac{2}{f}$ modes per network strand and equation (8) for the shear modulus of the phantom model the CMM predicts:

$$G_{\rm aff} = \frac{3}{2} \rho_{\rm strand} k_{\rm B} T \tag{14}$$

The junction affine model assumes that the surrounding molecules suppress the movements of the junction points so strongly that the latter's instantaneous positions (and not only their mean positions as in the case of the phantom model) change affinely with the shape of the sample. For the diamond networks this implies $\vec{R}_\lambda = \overleftrightarrow{\lambda}\ \vec{R}_1$ and $\vec{\Delta}_\lambda = \overleftrightarrow{\lambda}\ \vec{\Delta}_1$ and leads directly to equation (14). Note, that the affine model constitutes an *upper limit* for the modulus predicted from a classical theory.† In a first test [78] of the classical picture we have shown that the shear moduli of random IPDN exceed the affine limit, providing quantitative proof that one cannot calculate the elastic moduli from this ansatz. In this paper we present a more detailed comparison between our simulation results and the predictions of the constrained junction models.

2.6. The tube model

At present, the tube model of Edwards [24] and the reptation theory of de Gennes [48] are the most successful approach to the problem of entangled polymer systems [25]–[28]. The geometrical constraint is much easier to handle than the topological constraints discussed in the following section.

In section 2.1 we have discussed phantom networks where the strands between the $(f > 2)$-functional junction points are replaced by a entropic spring of strength k. In addition to the constraints on the motion of the junction points introduced in the previous section, the non-classical theories of rubber elasticity consider restrictions of the fluctuations of the strands *between the junction points* such as tubes or slip-links [11, 43]. It is easy to see that dividing the network strands into Gaussian sub-strands (i.e. formally introducing additional, two-functional junction points along the strands) changes nothing for a phantom network. The spring constant is doubled for a strand of half the original length, i.e. if an entropic spring of spring constant k is replaced by a linear sequence of N springs the latter have a spring constant of $N\,k$. Furthermore, the equilibrium positions of the new $(f = 2)$ functional cross-links are along the line connecting the equilibrium positions of the original endpoints. Since $\langle R_N^2\rangle = \frac{1}{N^2}\langle R^2\rangle$, one finds $k\,N\sum_{i=1}^{N}\langle R_N^2\rangle = k\langle R^2\rangle$ and the predicted modulus remains unchanged.†

The fluctuations of the strand conformations between the cross-links are most naturally analysed in terms of single chain Rouse-modes [25]. Duering *et al* [72, 75] have used this method to characterize the relaxation of entangled chains in (un)cross-linked melts [72, 75]. For the present purposes, it turns out to be convenient to regard the chain ends as fixed at $\vec{r}_0(t) \equiv \vec{R}_0$ and $\vec{r}_{N_{\rm strand}}(t) \equiv \vec{R}_{N_{\rm strand}}$ in contrast to the previously used open boundary conditions [72, 75]. One can then expand the deviations $\vec{u}_i(t) = \vec{r}_i(t) - \vec{R}_i$ from the equilibrium positions $\vec{R}_i = \vec{R}_0 + i/N_{\rm strand}\ \left(\vec{R}_{N_{\rm strand}} - \vec{R}_0\right)$ in terms of sin-Rouse-modes:

$$\vec{u}_p(t) = \frac{1}{N_{\rm strand}+1}\sum_{i=0}^{N_{\rm strand}} \vec{u}_i(t)\sin\left(\frac{p\pi i}{N_{\rm strand}}\right) \tag{15}$$

† The ratio $G_{\rm aff}/G_{\rm ph} = 3/2$ is an artifact of our choice of $\langle r^2\rangle^{1/2}$ for the bond length of the diamond lattice. In general, for an f-functional lattice one recovers the standard relation $G_{\rm aff}/G_{\rm ph} = \frac{f}{f-2}$ by setting $\vec{R}_1^2 = \frac{f-2}{f}\langle r^2\rangle$.
† Gao and Weiner [86] recently analysed the stress relaxation in a sheared melt of long-chain molecules along these lines from a sub-strand analysis. For many purposes this method is equivalent to the mode analysis. The latter offers the advantage of being compatible with the CMM and of naturally providing the length scales where entanglement effects become relevant.

$$\mathcal{H} = \frac{k}{2}\left(\vec{R}_0 - \vec{R}_{N_{\text{strand}}}\right)^2 + \sum_p \frac{k_p}{2}\vec{u}_p^2 \tag{16}$$

$$k_p = \frac{2\pi^2 k}{N_{\text{strand}}} p^2 \tag{17}$$

As the Einstein modes describe the fluctuations of the *junction points*, the Rouse modes (15) describe the fluctuations of the *monomers* around their respective equilibrium positions. Together the Einstein and the Rouse modes form a complete and orthogonal basis set. In particular, they are like the true eigenmodes of the phantom model *independent* of size and shape of the network and allow a simple distinction between classical and non-classical entanglement effects.

We can again use the CMM to discuss the consequences of a confinement of the Rouse modes due to entanglements. Consider the limit of long strands of $N_{\text{strand}} \to \infty$ Gaussian units, where the classical contribution to the shear modulus becomes negligible: $G_{\text{class}} \leq G_{\text{aff}} = \frac{\rho}{N_{\text{strand}}} k_{\text{B}}T \to 0$ (ρ here denotes the number density of the Gaussian units). The simplest ansatz for the p-dependence of the confinement parameter is a step function $\gamma_p = \Theta\left(p - \frac{N_{\text{strand}}}{N_{\text{e}}}\right)$, so that all modes with a wavelength larger than the entanglement length, N_{e}, are completely frozen. The shear modulus is obtained by multiplying the number of frozen modes per chain, $N_{\text{strand}}/N_{\text{e}}$, with the chain density ρ/N_{strand}:

$$G_{\text{tube}} = \frac{N_{\text{strand}}}{N_{\text{e}}} \frac{\rho}{N_{\text{strand}}} k_{\text{B}}T = \frac{\rho}{N_{\text{e}}} k_{\text{B}}T. \tag{18}$$

As already discussed in section 2.3, partially frozen modes with $0 < \gamma_p < 1$ lead to a weaker than affine deformations of both, the tube axes and the tube diameter, and to the characteristic Mooney–Rivlin corrections to the ideal stress–strain curves.

2.7. Topological theories of rubber elasticity

Already thirty years ago Edwards had outlined the two essential steps in a rigorous treatment of the topological constraints [7, 8]. The first step is the characterization of the state of the network in terms of an—in principle infinite—set of topological invariants. For example, the Gauss linking number (GLN)

$$I = \frac{1}{4\pi} \oint \oint \frac{(\mathrm{d}\vec{r}_1 \times \mathrm{d}\vec{r}_2) \cdot (\vec{r}_1 - \vec{r}_2)}{|\vec{r}_1 - \vec{r}_2|^3} = 0, \pm 1, \ldots \tag{19}$$

could be used to distinguish between entangled ($I \neq 0$) and non-entangled pairs of loops or meshes [87]. Although the use of the GLN is only justified for simple link topologies [87], it is the only topological invariant which can be incorporated into the standard polymer formalism [2, 87]

The second step is the calculation of the elastic response from quenched averages in which these invariants are conserved. Analytic attempts along these lines are very complex [2, 12, 13] even though they only take two-loop interactions into account. They require numerous and often uncontrolled approximations and no satisfactory treatment has been put forward so far. A principal problem in the development of topological theories is the question how they can be tested experimentally. At least to our knowledge, there is no experimental technique that could provide information on the microscopic topological state of a sample and thus help to test the validity of the underlying concepts. Computer simulations offer the unique possibility to overcome this difficulty. In fact, we chose the particular geometry of the IPDN with the intention

to determine the linking states of the meshes of these conveniently regular networks. Our analysis is based on [49] a theory which is complementary to the single-chain ansatz described above. The model of Graessley and Pearson [11] defines entanglements as links between closed loops (meshes) of the network. Their effects are included as additional entropic springs acting between the mesh centres of mass (CM). The effects on the strand conformations are ignored.

The underlying idea of an entropic interaction between two loops due to the conservation of their topological state was introduced by Vologodskii *et al* [37, 38]. Consider two rings of length N with CM distance $\vec{r}$. If the rings do not interact, then for all values of $\vec{r}$ the accessible phase space volume Ω is trivially given by the product of the phase space volumes of the individual rings. Naturally, there is no restoring force if the distance of the rings changes. The situation is different if topology conservation is introduced. The phase space becomes divided into disjunct regions for topologically equivalent conformations. To a first approximation, there are only two classes, linked and non-linked rings, so that $\Omega_{\mathrm{linked}}(\vec{r}) + \Omega_{\mathrm{non-linked}}(\vec{r}) = \Omega$. Consider the entropy of an ensemble of ring pairs which had a CM distance $\vec{r}_0$ when the topology conservation was introduced†. The probability that the rings are linked is given by $f(\vec{r}_0) = \Omega_{\mathrm{linked}}(\vec{r}_0)/\Omega$. The entropy of the ensemble, $S = f(\vec{r}_0)k_{\mathrm{B}}\log(f(\vec{r})) + (1 - f(\vec{r}_0))k_{\mathrm{B}}\log(1 - f(\vec{r}))$, thus not only depends on the actual ring distance $\vec{r}$ but also on $\vec{r}_0$. In fact, for small deviations from the original distance one can write $S(\vec{r}) = S(\vec{r}_0) - \frac{f'^2(\vec{r}_0)}{f(\vec{r}_0)(1-f(\vec{r}_0))}(r - r_0)^2$. While the individual ring pairs either attract or repel each other depending on whether or not they are linked, there is *on average* a (linear) restoring force to the state the members of the ensemble were in, when the topology was quenched.

For the chain length dependence of the linking probability one expects $f_N(r) = f(r/N^{1/2})$, even though $f(\vec{x})$ is not generally known. There are some rigorous results [88], approximative analytic treatments [89]–[91], [17], Monte Carlo simulations of pairs of closed random walks on a lattice [37, 38, 50, 88, 92], and our own results for the meshes of the diamond networks [49]. For finite N it turns out to be useful to define a 'linking radius' $\frac{4\pi}{3}R_{\mathrm{L}}^3 = \frac{1}{2}\int \mathrm{d}^3r\ f_N(\vec{r})$ and to consider $f_N(r) = f(r/R_{\mathrm{L}}(N))$ in order to reduce the finite size corrections to the scaled distribution function.

For loops which are randomly distributed in space with a density ρ_{loop} and a spherically symmetric linking probability one can define an entanglement (link) density:

$$\rho_{\mathrm{link}} = 2\pi\rho_{\mathrm{loop}}^2 R_{\mathrm{L}}^3 \int_0^\infty x^2\, f(x)\, \mathrm{d}x \quad . \tag{20}$$

In their attempt to estimate the topology contribution to the shear modulus of polymer networks Graessley and Pearson (GP) [11] assumed (1) that $f(\vec{x})$ remains unchanged under deformations of the sample, i.e. they ignored distortions of the loop shapes, (2) that the contributions of the different loop pairs are independent and additive, and (3) that the positions of the loop CM change affinely with the deformation $\overleftrightarrow{\lambda}$ of the sample. The loop contribution G_{link} to the shear modulus can be written in the form:

$$G_{\mathrm{link}} \quad = a[f(x)]\,\rho_{\mathrm{link}} \tag{21}$$

$$a[f(x)] = \frac{k_{\mathrm{B}}T}{15}\frac{\int_0^\infty \frac{x^4 f'^2(x)}{f(x)(1-f(x))}\,\mathrm{d}x}{\int_0^\infty x^2\, f(x)\,\mathrm{d}x}. \tag{22}$$

† In an experiment this is the moment when the second ring is closed; in our simulations it is the time we introduce the excluded volume interaction between all monomers (see section 3.5).

Under the assumption that—up to a prefactor a_0 of order one—the effect of topology conservation can be identified with $G_{\rm link}$, the total shear modulus G is given by:

$$G = G_{\rm ph} + a_0\, a[f(x)]\, \rho_{\rm link} \quad . \tag{23}$$

In this paper we provide more details of a quantitative test [49] of the model of Graessley and Pearson for random IPDN and discuss its applicability to the case of regular IPDN.

3. The simulation model

We use the same coarse-grained model as in earlier investigations of polymer melts and networks by Kremer and Grest [72, 75]. The polymers are modeled as freely jointed bead spring chains of uniform length N and are cross-linked into several, inter-penetrating networks with the connectivity of a diamond lattice. The systems are weakly coupled to a heat bath and relaxed in molecular dynamics simulations by integrating a Langevin equation. By varying the interaction potentials between the monomers we can simulate ensembles with or without topology conservation. They are characterized by the energy barrier U_{cross} for the mutual penetration of two chains. The networks reside in a cubic simulation box with periodic boundary conditions. Strain is introduced by stretching the simulation box in one direction with appropriate rescaling of the other two dimensions in order to conserve the volume. The latter is no serious restriction, since rubber typically has a Poisson ratio close to $\frac{1}{2}$.

3.1. Systems with conserved topology

For the excluded volume interaction between the monomers we usually use a Lennard–Jones (LJ) potential which is truncated in the potential minimum at $2^{1/6}\sigma$:

$$U_{\rm LJ}(r) = \begin{cases} 4\epsilon \left\{ \left(\frac{\sigma}{r}\right)^{12} - \left(\frac{\sigma}{r}\right)^{6} + \frac{1}{4} \right\} & r < 2^{1/6}\sigma, \\ 0 & r \geq 2^{1/6}\sigma. \end{cases} \tag{24}$$

σ and ϵ are the LJ units of length and energy. Time is measured in units of $\tau = \sigma\sqrt{\frac{m}{\epsilon}}$. Monomers additionally interact with their two (or, if they are cross-links, with their four) chemical neighbours via the an-harmonic FENE ('finite extendable non-linear elastic' [93]) potential:

$$U_{\rm FENE}(r) = \begin{cases} -\frac{30}{2}\frac{\epsilon R_0^2}{\sigma^2} \ln\left(1 - \left(\frac{r}{R_0}\right)^2\right) & \text{if } r < R_0, \\ \infty & \text{otherwise,} \end{cases} \tag{25}$$

with $R_0 = 1.5\sigma$. The energy barrier $U_{\rm Cross}$ for the mutual penetration of two chains can be estimated by considering two pairs of bonded monomers oriented perpendicular to each other and with a distance d between the centres of the bonds. For $d \to 0$ the bonds stretch. However, the energy barrier of $U_{\rm Cross} \approx 70 k_{\rm B}T$ is sufficiently high to ensure topology conservation in our simulations. We worked at a temperature $k_{\rm B}T = 1\epsilon$ and at a density $\rho = 0.85\sigma^{-3}$. The average bond length was $l = 0.97\sigma$. The relevant length and time scales for chains in a melt are the mean-square end-to-end distance $\langle R^2\rangle(N) \approx 1.7 l^2 N$, the melt entanglement length $N_{\rm e} \approx 35$ monomers, and the Rouse time [25] $\tau_{\rm Rouse} \approx 1.5 N^2 \tau$ [72].

3.2. Phantom chains

For comparison we also investigate two different ensembles without topology conservation but very similar static properties of the chains. To simulate phantom chains we restrict the LJ interaction to nearest and next nearest neighbour monomers along the chains. The chains can cross each other freely with $U_{\mathrm{Cross}} = 0$ and have a certain stiffness due to the next-nearest-neighbour interaction. The expectation value for the bond angle θ is given by:

$$\langle\cos(\theta)\rangle = \frac{\int_0^\pi \mathrm{d}\theta\ \sin(\theta)\cos(\theta)\mathrm{e}^{-U_{\mathrm{LJ}}(r(\theta))/k_{\mathrm{B}}T}}{\int_0^\pi \mathrm{d}\theta\ \sin(\theta)\mathrm{e}^{-U_{\mathrm{LJ}}(r(\theta))/k_{\mathrm{B}}T}} \approx 0.274\ , \tag{26}$$

where $r(\theta) = 2l\sin((\pi-\theta)/2)$ is the distance between next-nearest-neighbour monomers.

Since we do not count cross-links as next-nearest neighbours there are no restrictions on the first and last bond of each network strand. The mean-square end-to-end distance of two cross-links connected by a N monomer strand is given by

$$\begin{aligned}\langle r^2\rangle(N) &= 2l^2 + (N-1)l^2\times \\ &\quad\left(\frac{1+\langle\cos(\theta)\rangle}{1-\langle\cos(\theta)\rangle} - \frac{1}{N-1}\frac{2\langle\cos(\theta)\rangle(1-\langle\cos(\theta)\rangle^{N-1})}{(1-\langle\cos(\theta)\rangle)^2}\right) \\ &= c_N(N+1) = \begin{cases} 1.56l^2(N+1) & \text{for } N=12 \\ 1.66l^2(N+1) & \text{for } N=26 \\ 1.70l^2(N+1) & \text{for } N=44 \end{cases}\end{aligned} \tag{27}$$

Characteristic for the dynamics is the Rouse time

$$\tau_R^{(\mathrm{ph})} = \frac{\Gamma N^2 c_N l^2}{3\pi^2 k_{\mathrm{B}}T} = 0.054N^2\tau \quad . \tag{28}$$

For a friction constant $\Gamma = 1.0\tau^{-1}$ the monomer friction in the true melt is more than twenty times larger than the friction due to the coupling to the heat bath.

3.3. Systems with annealed topology

In order to calculate averages over an ensemble with annealed topology where polymer chains are able to cross each other [76], we replace the LJ-interaction with a 'soft-core' potential:

$$U_{\mathrm{SC}}(r) = \begin{cases} 4.44\epsilon & \text{if } r < \sigma, \\ 2.22\epsilon\left\{\cos\left(\frac{\pi(r-\sigma)}{(2^{1/6}-1)\sigma}\right)+1\right\} & \text{if } \sigma \le r \le 2^{1/6}\sigma, \\ 0 & \text{otherwise.} \end{cases} \tag{29}$$

R_0 in equation (25) is increased to 1.75σ. In contrast to the original investigations we here only reduced U_{FENE} and not the total interactions between neighbouring bonds by a factor 0.175. The energy barrier $U_{\mathrm{Cross}} \approx 4k_{\mathrm{B}}T$ is still low enough to allow the chains to penetrate each other so that an ensemble with variable or annealed topology is simulated. However, this involuntary modification may have contributed to the very long relaxation times we observed in the corresponding simulations. Even with this slight modification properties such as monomer packing, Rouse friction, pressure or strand persistence length remain practically unchanged compared to the simulations with the Lennard-Jones potential.

3.4. Diamond networks

We investigate model polymer networks with the connectivity of a diamond lattice. The regular structure was chosen to isolate the effects of topology conservation from other forms of quenched disorder, while we selected the diamond lattice for its four-functionality. In each diamond net polymer chains consisting of N monomers are initially arranged along the bond vectors of a diamond lattice. The cross-links are placed on the lattice sites and connected to end monomers of four chains. During the simulation the networks including the cross-links can move freely and the lattice structure is preserved only in the connectivity. The simulation box contains several, mutually inter-penetrating diamond nets, which are *not* chemically connected, but permanently entangled. The regular and defect free connectivity of the networks is especially suited for a comparison to topological theories of rubber elasticity. The following vector notation, while giving the initial spatial positions, is predominantly used in order to *label* the cross-links and chains in such a way that it becomes possible to identify the monomers forming an elementary mesh of the network.

The diamond lattice is a fcc lattice with a two-atom basis. Each unit cell contains 8 atoms and 16 bonds. The primitive cell is spanned by the three basis vectors $\vec{a}_1 = \frac{a}{2}(1,0,1)$, $\vec{a}_2 = \frac{a}{2}(1,1,0)$, $\vec{a}_3 = \frac{a}{2}(0,1,1)$, where a is the edge length of the unit cell. The two atoms of the basis are located at $(0,0,0)$ and $\frac{a}{4}(1,1,1)$. Atoms connected by covalent bonds are located on different sub-lattices. From each atom on the first sub-lattice there originate four bond vectors: $\vec{b}_1 = \frac{a}{4}(1,1,1)$, $\vec{b}_2 = \frac{a}{4}(1,1,-1)$, $\vec{b}_3 = \frac{a}{4}(1,-1,1)$, $\vec{b}_4 = \frac{a}{4}(-1,1,1)$. For atoms on the second sub-lattice the bond vectors have the opposite sign: $-\vec{b}_1, -\vec{b}_2, -\vec{b}_3, -\vec{b}_4$.

The meshes of the diamond lattice consist of six atoms and six bonds. A mesh can unambiguously be identified by choosing one atom on the first sub-lattice as the origin and a triple of pairwise different bond vectors for the first three bonds, e.g. $(\vec{b}_1, -\vec{b}_2, \vec{b}_3)$. In order to return to the origin, the same three bonds have to be used in the same order for the next three steps. The signs are inverted automatically, because the starting point for the second half is on the second sub-lattice. Thus, there are 24 possibilities per fcc lattice site. However, for a given mesh, one has the choice between three different atoms for the origin and a clockwise and counter-clockwise listing of the bonds. Eliminating the permutations in the order of bond vectors leaves four different meshes per fcc lattice site: $(\vec{b}_1, -\vec{b}_2, \vec{b}_3)$, $(\vec{b}_1, -\vec{b}_2, \vec{b}_4)$, $(\vec{b}_1, -\vec{b}_3, \vec{b}_4)$ and $(\vec{b}_2, -\vec{b}_3, \vec{b}_4)$. The number of meshes equals therefore the number of bonds and each bond is part of six meshes. Note, that it is not possible to partition the $16m^3$ bonds contained in m^3 fcc cells into a set of meshes without using some bonds more than once.

Polymer networks with diamond lattice connectivity are a straightforward extension of the Flory–Rehner tetraeder model. In this spirit we choose the edge length $a(N)$ so that the bond length equals the root-mean-square end-to-end distance of free chains of length $(N+2)$ (i.e. strand plus cross-links) in a melt:

$$a(N) = \frac{4}{\sqrt{3}} \sqrt{1.7(N+1)}\, 0.97\, \sigma \quad . \tag{30}$$

The monomer density of the diamond nets

$$\rho_{\mathrm{Net}}(N) = 8\frac{2N+1}{a^3(N)} \sim N^{-1/2} \quad , \tag{31}$$

is smaller than the melt density $0.85\sigma^{-3}$, so that a superposition of n independent diamond nets is required in order to reach this value. We refer to these structures as inter-penetrating diamond

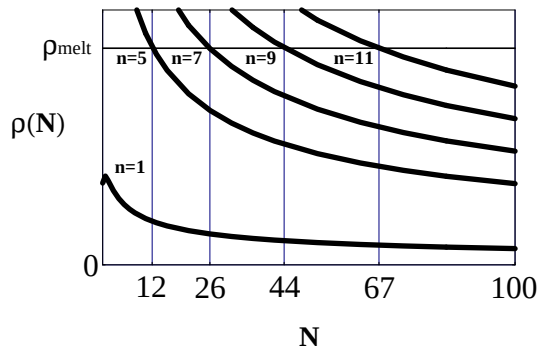

Figure 5. Strand length N dependence of the density of n inter-penetrating diamond nets under the condition equation (30).

Table 1. Investigated systems.

Strand length N	Diamond nets n	fcc cells $m \times m \times m$	Strands N_{ch}	Monomers N_{tot}
12	5	$2 \times 2 \times 2$	640	8000
12	5	$3 \times 3 \times 3$	2160	27000
26	7	$2 \times 2 \times 2$	896	23744
44	9	$2 \times 2 \times 2$	1152	51264

networks (IPDN). We use only systems which fulfil the condition $n\,\rho_{\mathrm{Net}}(N) \approx 0.85\sigma^{-3}$. Figure 5 shows that the investigated chain lengths of $N = 12, 26, 44$ correspond to $n = 5, 7, 9$ diamond nets. The total system size depends on the number of fcc cells in the simulation box. We used systems consisting of $2 \times 2 \times 2$ ($3 \times 3 \times 3$) cells, which corresponds to 64 (216) cross-links and 128 (432) strands per diamond net. Table 1 lists the investigated systems.

3.5. Regular and random inter-penetration

The topology of the systems depends on the preparation. We have investigated regular and random IPDN as examples for systems which are identical except for the topological constraints. As in experimental systems, spatial neighbour cross-links are usually not connected by a network strand. In our case they belong to different diamond nets. Their number n corresponds to the Flory number, which is defined as the number of cross-links in the volume of a network chain.

Simulations of regular IPDN start from intercalating conformations of strongly swollen networks with completely stretched strands. In MD runs the conformations are slowly compressed to melt density. The important point is that the topology conserving LJ interaction between all monomers is used right from the beginning.

The initial conformations for the random IPDN are set up at melt density. Between the cross-links on the diamond lattice sites we place phantom chains with the proper end-to-end

Table 2. Simulation times in units of τ of the investigated systems.

N		Phantom IPDN	Annealed IPDN	Random IPDN	Regular IPDN
12	$\lambda = 1.0$	500	4500	3000	3000
	$\lambda = 1.6$	500	6000	4500	4500
12	$\lambda = 1.0$	500	—	3000	3000
	$\lambda = 1.5$	—	—	4500	—
26	$\lambda = 1.0$	2000	15000	12000	12000
	$\lambda = 1.5$	—	15000	15000	15000
44	$\lambda = 1.0$	8000	15000	12000	12000
	$\lambda = 1.5$	8000	15000	15000	40000

distance. These phantom chains are generated in Monte Carlo simulations using the potentials defined above. After the relaxation of the lattice structure in MD runs for phantom chains, we introduce the repulsive excluded volume interaction between the monomers. This is done by slowly building up a cosine potential up to a point where the monomer distances are large enough for the LJ potential. From that point onwards the random topology is quenched [80]. The procedure is illustrated in video-sequence 1.

3.6. Simulation runs

The systems are weakly coupled to a heat bath and relaxed in molecular dynamics simulations by integrating a Langevin equation:

$$m\frac{\mathrm{d}^2\vec{r}_i}{\mathrm{d}t^2} = -\vec{\nabla}U_i - \Gamma\frac{\mathrm{d}\vec{r}_i}{\mathrm{d}t} + \vec{W}_i(t) \quad . \tag{32}$$

$\vec{r}_i$ is the position of the ith monomer with mass m, U_i its potential energy and $\vec{W}_i$ a random force with $\langle\vec{W}_i(t)\rangle = 0$ and whose strength is related by the fluctuation-dissipation theorem to the friction constant Γ and the temperature T: $\langle\vec{W}_i(t)\cdot\vec{W}_j(t')\rangle = 6k_\mathrm{B}T\Gamma\delta_{ij}\,\delta(t-t')$. The time step for the integration was 0.01τ. The program was vectorized for the Cray YMP using the grid search algorithm [94] for the excluded volume interactions. The performance was about 3×10^6 particle updates per second.

To facilitate the deformation of the simulation box we internally represent the coordinates as reduced vectors in a unit cube $[-1/2, 1/2]^3$. The true distances are calculated using a metric $L^2\overset{\leftrightarrow}{\lambda}^t\overset{\leftrightarrow}{\lambda}$, where L is the edge length of the unstrained simulation box. In our simulations we consider volume-conserving uni-axial elongations by a factor of λ along the x-axis (equation (3)), the standard deformation treated in theories of rubber elasticity. In runs with $\lambda \neq 1$ the strain is introduced at the beginning as a sequence of small deformations. Subsequently we perform relaxation runs of the order $10\tau_\mathrm{Rouse}(N)$ (table 2). Particle coordinates are stored on tape every 30–50 τ depending on the strand length.

Table 3. Internal energies in units of ϵ in the strained and unstrained state.

N		Phantom IPDN	Annealed IPDN	Random IPDN	Regular IPDN
12	$\lambda = 1.0$	16703	27123	19760	19784
	$\lambda = 1.6$	16726	27117	19763	19787
12	$\lambda = 1.0$	56358	—	66736	66766
	$\lambda = 1.5$	—	—	66714	—
26	$\lambda = 1.0$	49443	80729	58590	58634
	$\lambda = 1.5$	—	80722	58582	58634
44	$\lambda = 1.0$	106629	174468	126426	126520
	$\lambda = 1.5$	106628	174454	126416	126511

4. Results

4.1. Entropic origin of the network elasticity

Of immediate interest in the analysis of computer simulations of strained model polymer networks is the behaviour of the internal energy. The values listed in table 3 demonstrate that for elongations of the samples of the order of 50% the internal energy is virtually identical to the unstrained state. This holds for phantom IPDN† as well as for IPDN with conserved and annealed topology. The strain invariance of the internal energy implies that our model systems show ideal rubber elasticity with restoring forces exclusively due to a change of entropy. While this agrees with most experiments, we note that the absence of enthalpic contributions is not built into the model. In principle, elastic energy can be stored in the springs connecting the beads. However, this effect only comes into play for large deformations (see figure 4 and the second video sequence 6) when the chains are nearly stretched to their full contour lengths.

4.2. Stress relaxation in deformed networks

To follow the relaxation of the normal stresses we calculate the pressure tensor using a formulation of the virial theorem where only the relative particle positions enter [95]:

$$\overleftrightarrow{\sigma}\ V = \sum_i m_i \vec{v}_i \otimes \vec{v}_i + \sum_{\langle i<j \rangle} \frac{\vec{r}_{ij} \otimes \vec{r}_{ij}}{r_{ij}} \left(\frac{\mathrm{d}\, U_{\mathrm{FENE}}(r)}{\mathrm{d}r} \right)_{r=r_{ij}}$$

† The only system which displays a small increase in the internal energy under strain is the phantom IPDN with $N = 12$. This might be related to the comparatively strong finite chain length effects we observed for this systems in general. In all other cases the energy differences, when converted into an estimate for the energetic contribution to the shear modulus, are of the order of $|G_U| < 0.001\epsilon/\sigma^3$, which is less than our error estimate for the measured shear moduli.

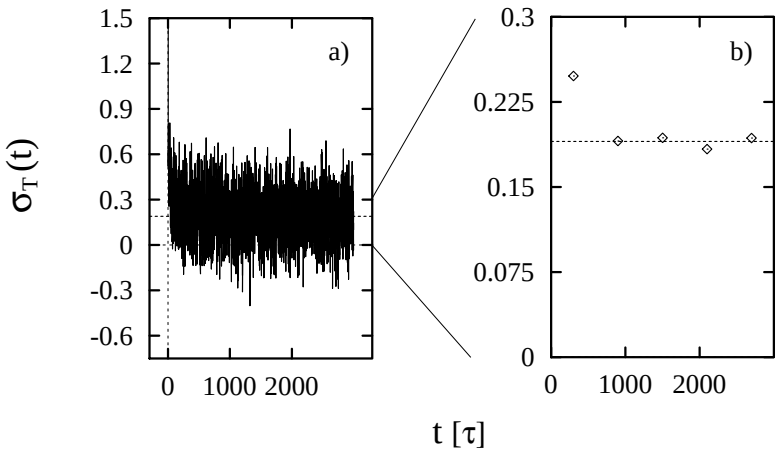

Figure 6. Stress relaxation for random IPDN with $N = 12$ after an elongation of 60%: (a) the original data; (b) after averaging over blocks of a width of 600τ. The Rouse time for the strands is about 220τ.

$$+ \sum_{i<j} \frac{\vec{r}_{ij} \otimes \vec{r}_{ij}}{r_{ij}} \left(\frac{\mathrm{d}\, U_{\mathrm{LJ}}(r)}{\mathrm{d}r} \right)_{r=r_{ij}} \quad . \tag{33}$$

Figure 6 shows a typical result for the relaxation of the normal stress

$$\sigma_T = \sigma_{xx} - \tfrac{1}{2}(\sigma_{yy} + \sigma_{zz}) \quad , \tag{34}$$

to an asymptotic value. We find that even for a deformation of 60% the induced normal stress of 0.2 ϵ/σ^3 is smaller than the width of the thermal fluctuations, so that a very long averaging is required. In particular, it is not possible to determine normal stresses for strains that are small enough to allow the application of linear elasticity theory. For the simulation times listed in table 2 the stress relaxation is completed after the first quarter of the runs. Conformations stored during this period were discarded for the analysis of equilibrium properties in the strained state.

Experimental stress–strain curves usually follow the classical prediction [1] $\sigma_T = G(\lambda^2 - 1/\lambda)$ for elongations up to between 50 and 100%. Figure 7 shows that this is also the case for our model systems, at least for the case of $N = 12$. We also note the good agreement between the results for large and the small random IPDN with $N = 12$, which indicate that neither the system size nor the disorder average is critical. Due to the long simulation times we restricted ourselves for the larger systems to $\lambda = 1.5$. The elongation is sufficiently strong to provoke a measurable response outside the statistical noise and should still be inside the neo-Hookean regime. The shear moduli G listed in table 8 were determined with good accuracy from the slope of a straight line neglecting possible corrections of the Mooney–Rivlin type to the ideal stress–strain relation. Note that this approximation tends to *underestimate* the small-strain shear moduli. Finally we mention a peculiarity of the regular IPDN. These systems have a small negative normal stress in the unstrained state, but the observed stresses for finite strain still fall onto a straight line when plotted as in figure 7.

The values found for the shear moduli of phantom, annealed, and—quite interestingly— of regular IPDN show a remarkable agreement and display the $1/N$-behaviour expected from the classical theories (figure 8). Slightly increased values are found for the short phantom chains and the regular IPDN with $N = 44$. In the first case, the deviations are a little higher than

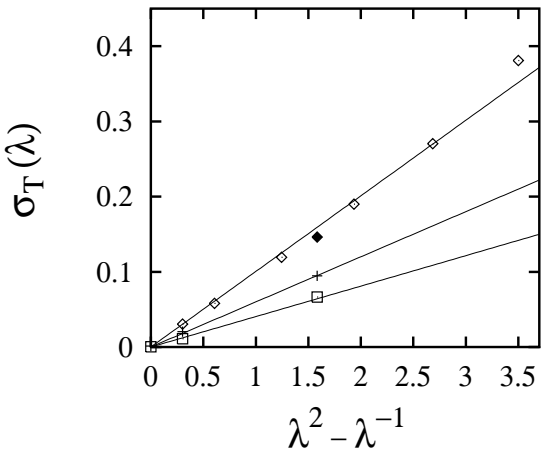

Figure 7. Stress–strain curves for random IPDN: $N = 44$ (squares), $N = 26$ (+), ($N = 12$) ($\diamond$). The filled symbol represents a measurement for the large system with $N = 12$.

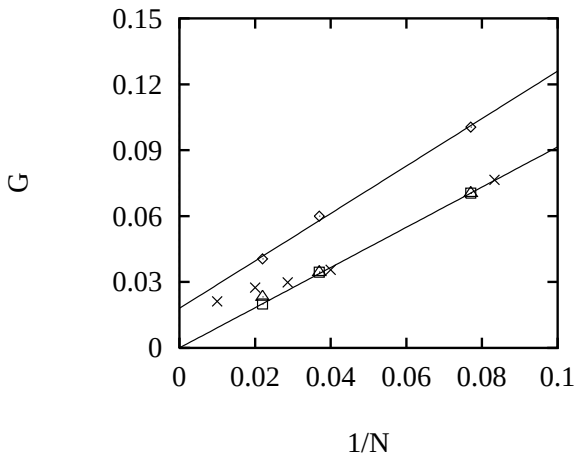

Figure 8. Strand length dependence of the shear moduli of IPDN: random IPDN ($\diamond$), regular IPDN ($\triangle$) and IPDN with annealed topology (squares). The solid line shows the prediction of the phantom model, the dashed line a rough extrapolation of the results for random IPDN to infinite strand length. For comparison we have included results of the mode analysis for end-linked melts [77, 75] ($\times$).

expected from the stiffness equation (27) of the phantom chains. The good agreement between the results for phantom and annealed IPDN confirms theoretical considerations that excluded volume interactions as such do not contribute to the elastic response [96].

That the conserved topology in regular IPDN has such a small effect on the shear modulus is an interesting effect in itself. The deviations from the phantom model for the largest strand length, $N = 44 > N_e$ are just outside our estimated margins of error. No reliable extrapolation is possible to the limit $N \to \infty$.

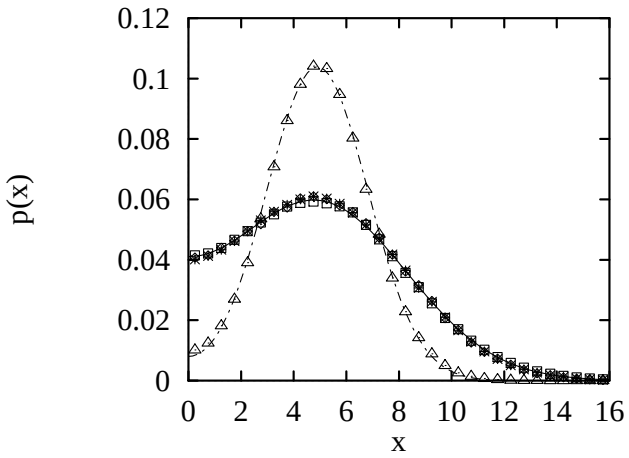

Figure 9. Probability distribution for one Cartesian coordinate of the strand end-to-end distances in IPDN with $N = 44$: random (squares), regular ($\triangle$), annealed ($*$) and phantom ($\diamond$) IPDN. The lines are fits to equation (7). The parameters are listed in table 4. For clarity, we included only the x-component for regular IPDN.

For the random IPDN we find significantly higher shear moduli than for the other systems. The entanglement contribution to the modulus

$$\frac{G_{\text{rand. IPDN}} - G_{\text{ph}}}{G_{\text{rand. IPDN}}} = \begin{cases} 0.30 \pm 0.03 & \text{for } N = 12 \\ 0.42 \pm 0.04 & \text{for } N = 26 \\ 0.49 \pm 0.05 & \text{for } N = 44 \end{cases} \tag{35}$$

is very high even for $N < N_{\text{e}}$. In contrast to the predictions of the classical models, the shear moduli of the random IPDN do *not* extrapolate to zero (figure 8) but to a finite value $G(N \to \infty) = 0.018 \pm 0.03\,\epsilon/\sigma^3$. This value is higher, but comparable to the mode analysis result for end-linked melts [77, 75] (figure 8). The close relation to the viscoelasticity of long chain polymer melts becomes clear from an estimate of the plateau modulus from the entanglement length $N_{\text{e}} = 35$ found in the corresponding melt simulations [72]. In a crude approximation one could map the entangled melt onto a network with four-functional cross-links and strands of length N_{e} and estimate the modulus from the classical models of rubber elasticity, obtaining predictions between $G_{\text{ph}}(N_{\text{e}}) = 0.012\,\epsilon/\sigma^3$ and $G_{\text{aff}}(N_{\text{e}}) = 0.024\,\epsilon/\sigma^3$ respectively.

4.3. End-to-end distance distributions of the network strands

The classical theories of rubber elasticity calculate the elastic response from the entropy change of the network strands, i.e. from the change of the strand end-to-end distance distribution in the deformed sample. In contrast to experiments these distributions are directly observable in a computer simulation.

Due to the discrete symmetry of the diamond lattice we always consider the probability distributions $p(x)$, $p(y)$ and $p(z)$ for one Cartesian coordinate. For linear chains the spatial distribution is given by $p(\vec{r}) = p(x)p(y)p(z)$. Since the orientation of the chains and hence the sign of x is irrelevant, we measure $p(|x|)$ etc. Figure 9 demonstrates the agreement of the network structure for the phantom, annealed and random IPDN, indicating that our preparation

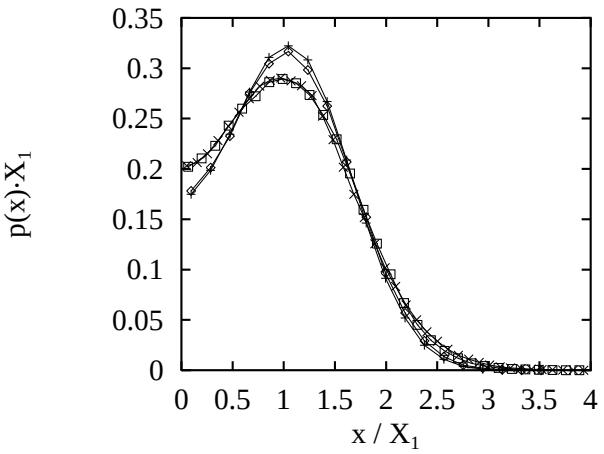

Figure 10. Scaled probability distribution for one Cartesian coordinate of the strand end-to-end distances in random IPDN: $N = 44$ ($\times$), $N = 26$ (squares), $N = 12$, $2 \times 2 \times 2$ fcc cells ($\diamond$), $3 \times 3 \times 3$ fcc cells (+). The scaling length X_1 was set to $1/\sqrt{3}$ times the bond length in the original diamond lattice.

methods generate well relaxed conformations. In the case of regular IPDN the distributions are narrower with smaller fluctuations in the x- than in the y- and z-directions. The reason for this asymmetry is the packing along the x-axis of the individual diamond nets.

It is important to note that the distributions are not peaked around $x = 0$ as would be the case in a (randomly cross- or end-linked) melt. To an excellent approximation they have the form equation (7) of a superposition of two Gaussian distributions of width Δ_λ^x around some peak position $\pm X_\lambda$. The suitably normalized fit parameters are listed in table 4. In the unstrained state the peak positions X_1 are in all systems given by the preset bond length of the diamond lattice equation (30) with $X_1 \approx \pm a(N)/4 \sim N^{0.5}$ (figure 10). The phantom model prediction for the width of the distributions in a network with $f = 4$ functional cross-links is [6] $(\Delta_\lambda^x)^2 = \frac{1}{3}\frac{2}{f}\langle r^2 \rangle$. For $N = 44$ this relation is indeed observed for phantom, annealed, and random IPDN. For shorter strands the distributions are slightly narrower than expected. There are two likely reasons: (1) deviations of the stiffness of the phantom chains *during the preparation of the networks* (equation (27)) from the uniform value $c_N = 1.7$ that we assumed for the construction of the networks and (2) deviations from the ideal behaviour *in the cross-linked melt* due to the finite strand length. For $N = 12$ the second aspect seems to play a role. The comparison of two systems composed of $2 \times 2 \times 2$ and $3 \times 3 \times 3$ fcc cells shows that the finite *system* size has no major effects.

Figure 11 shows one example for the distributions in the strained networks. In agreement with the predictions of all classical models the peak positions transform affinely, i.e. to $X_\lambda = \lambda X_1$ and $Y_\lambda = Y_1/\sqrt{\lambda}$ respectively. More interesting is the behaviour of the widths $\vec{\Delta}_\lambda$. For regular and random IPDN we find the expected crossover from phantom ($\vec{\Delta}_\lambda = \vec{\Delta}_1$) to affine ($\vec{\Delta}_\lambda = \overleftrightarrow{\lambda}\, \vec{\Delta}_1$) behaviour. The phantom and annealed IPDN show again some artifacts. Only for the phantom IPDN with $N = 44$ $\vec{\Delta}_\lambda$ remains unchanged as expected from the phantom model. The reduction of the fluctuations parallel to the elongation in the case of the phantom IPDN with $N = 12$ is additional evidence for non-Gaussian behaviour of the short strands. The deviations in the case of annealed IPDN indicate that due to the extremely long relaxation times it is not

Table 4. Fit results for the peak positions $X_\lambda, Y_\lambda, Z_\lambda$ of the end-to-end distance distributions (equation (7)) normalized to the preset bond length $a(N)/4$ of the diamond lattice. The second $N = 12$ systems consists of $3 \times 3 \times 3$ fcc unit cells. Results marked with * refer to runs with $\lambda = 1.6$. For comparison: $1.5^{-1/2} \approx 0.82$ and $1.6^{-1/2} \approx 0.80$.

		Phantom IPDN		Annealed IPDN		Random IPDN		Regular IPDN	
N		$\lambda = 1.0$	1.5	1.0	1.5	1.0	1.5	1.0	1.5
12	x	1.01	1.63*	1.01	1.52	1.03	1.65*	1.00	1.61*
	y	1.01	0.80*	1.02	0.83	1.03	0.80*	1.01	0.80*
	z	1.01	0.80*	1.02	0.83	1.02	0.80*	1.00	0.80*
12	x	1.01	—	—	—	1.02	1.53	1.01	—
	y	1.01	—	—	—	1.02	0.83	1.01	—
	z	1.01	—	—	—	1.02	0.83	1.01	—
26	x	1.00	—	1.01	1.51	1.02	1.54	1.01	1.51
	y	1.00	—	1.01	0.82	1.01	0.82	1.00	0.82
	z	1.00	—	1.01	0.82	1.00	0.82	1.01	0.82
44	x	1.00	1.51	1.00	1.51	1.00	1.51	1.00	1.51
	y	1.00	0.82	1.00	0.82	1.00	0.83	1.00	0.82
	z	1.00	0.82	1.00	0.82	1.00	0.82	1.00	0.82

possible to fully equilibrate these systems.

Constrained junction models (see section 2.5) try to predict the distributions plotted in figure 11 from an analysis of the Einstein modes in the unstrained state. Since these modes describe the displacement of the cross-links from their mean positions *in the absence of topological constraints* (i.e. in the corresponding phantom network), the analysis is not completely straightforward. To avoid ambiguities with the centre of mass degree of freedom of the whole network, it might be advantageous to instead consider the fluctuations in the end-to-end distances of the network strands around their equilibrium extensions in the corresponding phantom network. As the Einstein modes for the two endpoints of a strand are supposed to be independent, there is just a factor of two between the two results. For the present diamond networks this trick is especially convenient, because we know the equilibrium extensions of the strands (the bond vectors (x_1, y_1, z_1) in the underlying diamond lattice) from the construction of the networks.

Figure 12 shows the auto-correlation functions $c(t)$ of the Einstein modes for the different types of diamond networks under investigation. For phantom, annealed and regular IPDN $c(t)$ decays to zero: the mean cross-link positions are lattice sites of the original diamond lattice. As a consequence the systems are ergodic, i.e. sampling the end-to-end distance distributions for individual strands from a long time trajectory would yield the ensemble averages in tables 4 and 5. For phantom and annealed IPDN this is almost trivial to note, except that one has to be aware of the extremely long relaxation times in the latter case, which exceed our simulation times.

Table 5. Fit results for the width of the end-to-end distance distributions $(\Delta_\lambda^{\{x,y,z\}})^2$ (equation (7)) normalized to the expectation value $\frac{1}{3}\frac{2}{f}\langle r^2\rangle$. The second $N = 12$ systems consists of $3 \times 3 \times 3$ fcc unit cells. Results marked with * refer to runs with $\lambda = 1.6$.

		Phantom IPDN		Annealed IPDN		Random IPDN		Regular IPDN	
N		$\lambda = 1.0$	1.5	1.0	1.5	1.0	1.5	1.0	1.5
	x	0.75	0.63*	0.72	0.56	0.78	0.92*	0.36	0.40*
12	y	0.79	0.75*	0.70	0.56	0.83	0.77*	0.47	0.36*
	z	0.78	0.81*	0.65	0.62	0.83	0.65*	0.48	0.36*
	x	0.77	—	—	—	0.77	0.85	0.37	—
12	y	0.75	—	—	—	0.79	0.67	0.47	—
	z	0.76	—	—	—	0.76	0.63	0.48	—
	x	0.87	—	0.83	0.74	0.96	1.49	0.35	0.42
26	y	0.88	—	0.82	0.67	0.91	0.73	0.51	0.39
	z	0.89	—	0.85	0.73	1.03	0.78	0.51	0.39
	x	0.94	0.93	0.97	1.12	0.97	1.75	0.31	0.40
44	y	0.91	0.93	0.93	0.77	0.97	0.73	0.46	0.39
	z	0.94	0.95	0.87	0.71	0.93	0.77	0.48	0.38

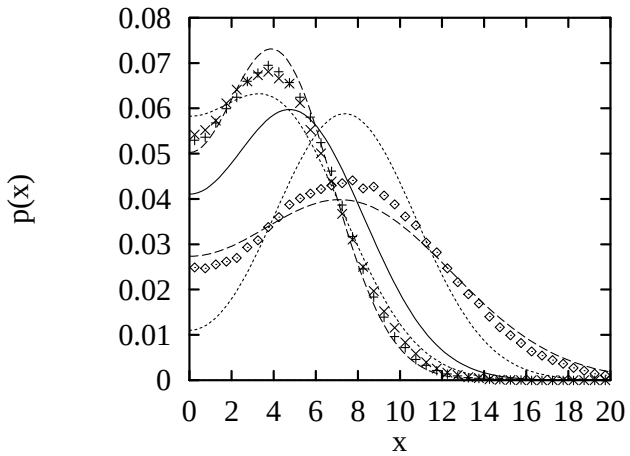

Figure 11. Probability distribution for one Cartesian coordinate of the strand end-to-end distances in random IPDN with $N = 44$ after an elongation of the sample by a factor of $\lambda = 1.5$ in x-direction: $p(x)$ ($\diamond$), $p(y)$ (+) and $p(z)$ ($\times$). The lines mark the distribution in the unstrained state (——) and the predictions of the phantom ($\cdots$) and of the affine (– – –) model.

For regular IPDN the mean cross-link positions remain unchanged due to symmetry, since the conserved topology is identical for all strands. In this case, the effect of the constraints is to

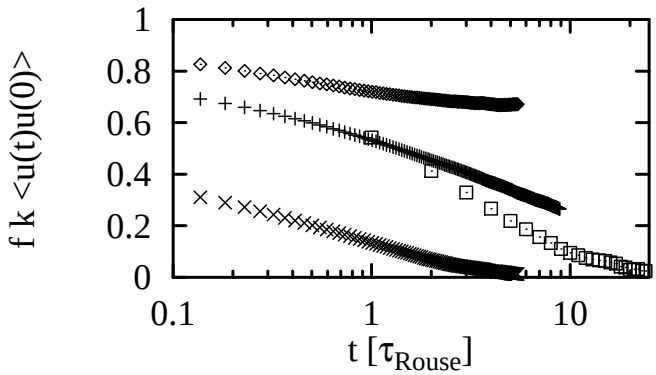

Figure 12. Auto-correlation function of the Einstein modes in IPDN with $N = 26$: phantom (squares), annealed (+), regular ($\times$) and random ($\diamond$) IPDN.

decrease the fluctuations compared to the phantom networks:

$$\gamma_{||} = 1 - fk\left\langle \delta u_x^2 \right\rangle = \begin{cases} 0.52 \pm 0.05 & \text{for } N = 12 \\ 0.61 \pm 0.05 & \text{for } N = 26 \\ 0.67 \pm 0.05 & \text{for } N = 44 \end{cases}$$

$$\gamma_{\perp} = 1 - fk\left\langle \delta u_{y,z}^2 \right\rangle = \begin{cases} 0.38 \pm 0.05 & \text{for } N = 12 \\ 0.42 \pm 0.05 & \text{for } N = 26 \\ 0.49 \pm 0.05 & \text{for } N = 44 \end{cases}$$

where $\langle \delta u^2 \rangle = \frac{1}{2}(\Delta_1^{\{x,y,z\}})^2$.

In contrast, the auto-correlation functions of the Einstein modes in random IPDN do not decay to zero. The topological constraints cause a limitation of the movement of the individual junction points which is stronger, but comparable to the case of regular IPDN. With increasing strand length, the systems show a crossover from phantom model ($\gamma = 0$) to the limit of the affine model with ($\gamma = 1$):

$$\gamma = \lim_{t\to\infty} \frac{\langle u(t)u(0)\rangle}{\langle u^2\rangle} = \begin{cases} 0.63 \pm 0.05 & \text{for } N = 12 \\ 0.71 \pm 0.05 & \text{for } N = 26 \\ 0.77 \pm 0.05 & \text{for } N = 44. \end{cases} \tag{36}$$

As a consequence, the mean extension of the individual chains is no longer given by x_1. Rather, there is a distribution of mean extensions with a maximum at this position and a finite width $2\gamma\frac{k_B T}{fk}$.

4.4. Mode analysis

In order to go beyond the classical theories of rubber elasticity one needs to take the limited fluctuations along the entire strand contour into account. We try to quantify this effect by analysing the conformations of network strands and of long, random paths ($N_{\text{path}} = 200$) through the network in terms of single-chain Rouse modes. At this point we concentrate on the asymptotic limit of the mode auto-correlation functions and on the distributions of mode

Table 6. Excitation of the first ten strand modes for IPDN with $N = 44$. γ_p is the degree of confinement with an uncertainty of the order of up to 10% for the longest mode. The fluctuations width are normalized to the theoretical values for Gaussian chains: $k_p\langle u_p^2\rangle$. The ratio $\alpha = 1/2(\langle y_p^2\rangle + \langle z_p^2\rangle)/\langle x_p^2\rangle$ measures the increase in the effective spring constant for fluctuations parallel to the elongation.

		$\lambda = 1.0$				$\lambda = 1.5$			
Mode	p	γ_p	x	y	z	x	y	z	α
	1	0.0	0.89	0.89	0.90	0.85	0.90	0.91	1.06
	2	0.0	0.90	0.90	0.89	0.86	0.88	0.89	1.02
	3	0.0	0.89	0.88	0.88	0.85	0.86	0.87	1.01
	4	0.0	0.87	0.87	0.88	0.85	0.86	0.87	1.01
Phantom	5	0.0	0.86	0.87	0.86	0.83	0.87	0.87	1.05
IPDN	6	0.0	0.85	0.86	0.84	0.80	0.86	0.87	1.08
	7	0.0	0.83	0.84	0.83	0.81	0.83	0.84	1.03
	8	0.0	0.81	0.82	0.81	0.78	0.81	0.80	1.03
	9	0.0	0.81	0.80	0.79	0.77	0.80	0.80	1.04
	10	0.0	0.79	0.79	0.79	0.76	0.78	0.79	1.04
	1	0.0	0.90	0.90	0.93	0.86	0.85	0.84	0.99
	2	0.0	0.87	0.88	0.88	0.82	0.89	0.86	1.06
	3	0.0	0.84	0.85	0.86	0.79	0.84	0.84	1.07
	4	0.0	0.82	0.82	0.82	0.77	0.82	0.82	1.06
Annealed	5	0.0	0.79	0.79	0.79	0.76	0.80	0.80	1.05
IPDN	6	0.0	0.78	0.77	0.77	0.74	0.78	0.78	1.05
	7	0.0	0.75	0.75	0.75	0.72	0.76	0.76	1.05
	8	0.0	0.73	0.73	0.73	0.71	0.74	0.74	1.04
	9	0.0	0.72	0.72	0.71	0.69	0.72	0.72	1.04
	10	0.0	0.70	0.70	0.70	0.68	0.71	0.70	1.04
	1	0.64	1.16	1.18	1.09	1.49	0.99	0.96	0.66
	2	0.39	1.14	1.18	1.13	1.21	1.06	1.07	0.88
	3	0.20	1.04	1.05	1.05	1.01	1.02	1.00	1.00
	4	0.09	0.95	0.95	0.95	0.89	0.95	0.93	1.05
Random	5	0.04	0.86	0.86	0.87	0.81	0.86	0.87	1.06
IPDN	6	0.02	0.81	0.81	0.81	0.75	0.80	0.81	1.07
	7	0.01	0.75	0.76	0.76	0.71	0.76	0.76	1.07
	8	0.005	0.72	0.72	0.72	0.68	0.73	0.73	1.07
	9	0.001	0.69	0.69	0.69	0.65	0.70	0.69	1.07
	10	0.002	0.67	0.67	0.67	0.63	0.67	0.67	1.06
	1	0.2	0.77	0.68	0.68	0.85	0.63	0.61	0.73
	2	0.01	0.87	0.90	0.90	0.85	0.86	0.85	1.00
	3	0.0	0.88	0.87	0.87	0.84	0.85	0.85	1.01
	4	0.0	0.88	0.88	0.87	0.83	0.87	0.87	1.04
Regular	5	0.0	0.86	0.85	0.86	0.82	0.85	0.86	1.04
IPDN	6	0.0	0.84	0.84	0.84	0.80	0.84	0.84	1.05
	7	0.0	0.82	0.82	0.81	0.78	0.82	0.82	1.05
	8	0.0	0.79	0.79	0.80	0.76	0.80	0.80	1.05
	9	0.0	0.77	0.77	0.77	0.74	0.77	0.78	1.05
	10	0.0	0.75	0.75	0.75	0.72	0.75	0.76	1.05

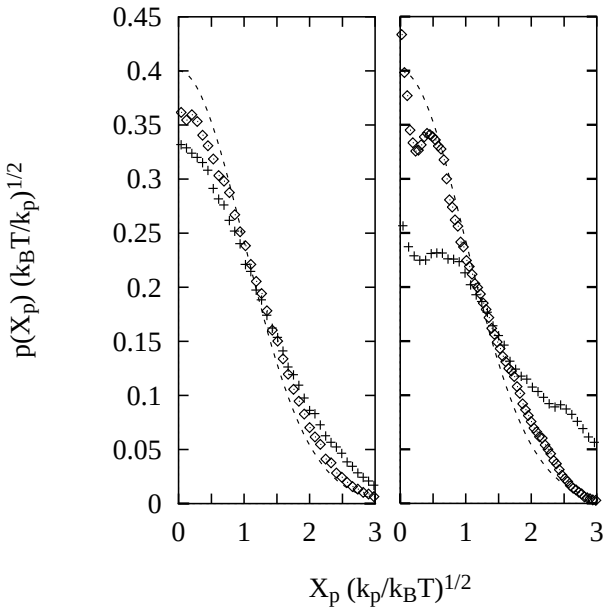

Figure 13. Scaled probability distribution for the first strand and path mode in random IPDN with $N = 44$. ($\diamond$ for $\lambda = 1.0$ and + for $\lambda = 1.5$). The dashed line indicates a standard Gaussian distribution.

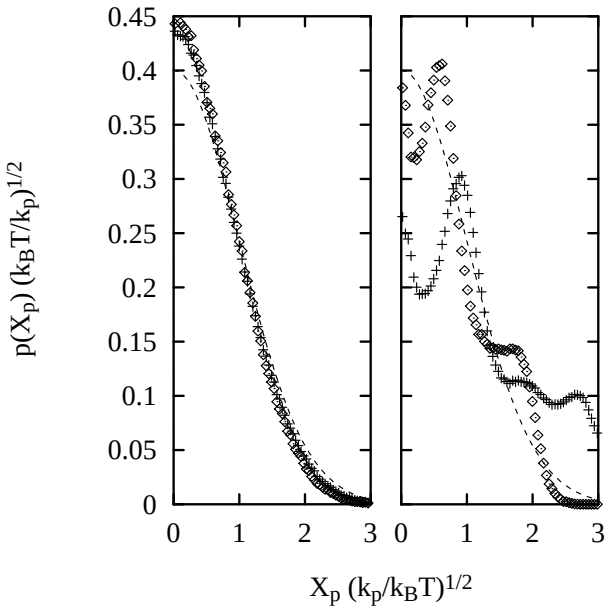

Figure 14. Scaled probability distribution for the first strand and path mode in regular IPDN with $N = 44$. ($\diamond$ for $\lambda = 1.0$ and + for $\lambda = 1.5$).

excitations in strained and unstrained networks. An explicit comparison to the CMM will be presented in Section 5.2.

Figures 13 and 14 show why, for diamond networks in particular, the strand modes are much more useful than the path modes ($N_{\text{path}} = 200$) which were employed for randomly cross- and

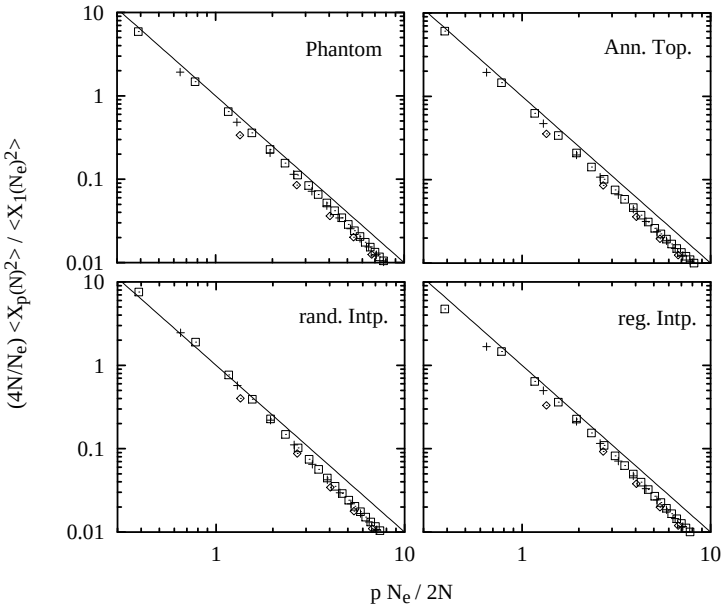

Figure 15. Mean squared excitation of the strand modes in the four different systems: $N = 44$ (squares), $N = 26$ (+), $N = 12$ ($\diamond$). The straight line indicates the theoretical predictions for a Gaussian chain.

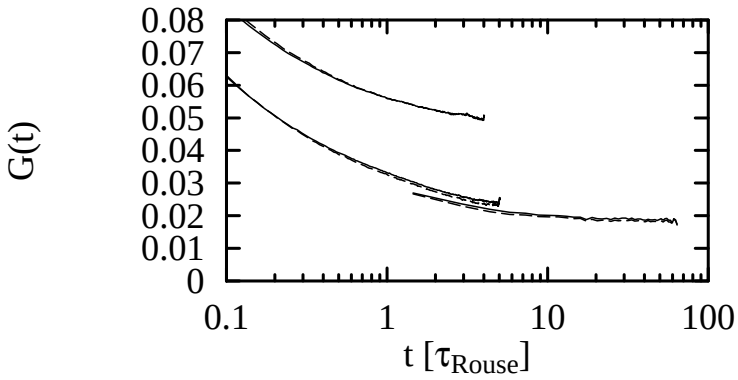

Figure 16. Comparison of the shear relaxation moduli as obtained from the path (– – –) and the strand (——) mode analysis for $N = 44$. The three pairs (!) of curves were obtained for (from top to bottom) random, annealed, and phantom IPDN.

end-linked melts [75, 76]. As we pointed out in section 2.6, the excitations of the strand modes for a Gaussian chain are independent of the chain's end-to-end distance. The strand modes therefore avoid artifacts due to the lattice connectivity and the pre-stretching of the strands (see figure 10). In contrast, for the path modes the lower modes with a wavelength exceeding the strand length are not normally distributed. Moreover, and in contrast to the strand modes, the path modes are strain dependent even in systems without topological constraints where they just provide a complicated way of measuring the phantom network modulus. In systems with conserved topology their analysis introduces unnecessary complications and below we shall concentrate

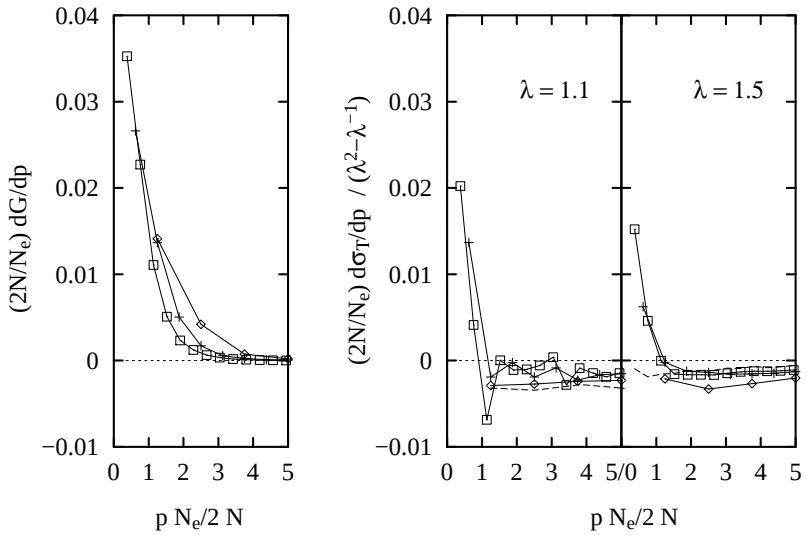

Figure 17. Contribution of different modes to the shear modulus $G_{\rm tube}$ and to the normal stress in elongated random IPDN: $N = 44$ (squares), $N = 26$ (+), ($N = 12$) ($\diamond$). The dashed lines show the apparent normal stresses in strained phantom networks with $N = 12$ for $\lambda = 1.1$ and with $N = 44$ for $\lambda = 1.5$.

on the strand modes. It seems, however, worthwhile to mention that one obtains identical (but incorrect, see figure 22c) predictions for the shear relaxation modulus using the strand and the path modes in the mode analysis suggested by Duering *et al* [75] (Figure 16).

Figure 15 and table 6 show a comparison between the observed ensemble averages for the distribution widths and the Rouse model prediction equation (16) for the strand modes.† The general agreement is very good in all four cases with the deviations for the higher modes being due to the non-Gaussian character of our chains (modes with $p\frac{2N}{N_e} = 5$ correspond to excitations where every 3rd or 4th monomer is moved in opposite directions). The only interesting exception are the longest wavelength modes of the regular IPDN, which are suppressed and anisotropic. The interpretation is the same as for the fluctuations of the end-to-end distances discussed in the previous section. Note that here the fluctuations in x-direction are *enhanced*.

The CMM suggest a close relation between the confined fluctuations in the unstrained state and the mode excitations in a strained sample. While one expects the case of phantom and annealed IPDN to be trivial, some complications arise due to the non-Gaussian character of the model polymers which are also relevant to the other cases.

For phantom and annealed IPDN the auto-correlation functions, $c_p(t)$, of the Rouse modes decay to zero. Thus, as expected, the strands are not permanently constrained and the modes do not have finite mean excitations (figure 20 documents this indirectly by the vanishing of the CMM expression equation (13) for the shear relaxation modulus, which is the sum of the squared, normalized mode auto-correlation functions). What is unexpected, at least for Gaussian chains, is the slight anisotropy of the modes in stretched networks (table 6) due to a reduction of the fluctuations parallel to the elongation. As a consequence, one formally finds a p-independent

† In this and the following figures we have rescaled the mode numbers in such a way that $p\frac{2N}{N_e} = 1$ corresponds to a mode with a wavelength equal to the melt entanglement length $N_e = 35$ monomer. In this manner the results for different strand lengths N can be conveniently compared.

negative contributions from all modes to the normal stress (equation (5), figure 17), which is clearly unphysical. The effect is more pronounced for short than for long chains. Its origin lies in the anisotropy of the fluctuations of stretched polymers with a well-defined contour length. The simplest case is the freely jointed chain, where the reduction of the fluctuations parallel to the elongation scales with the ratio of the mean chain extension to the chain contour length. In the present case of a chain of connected Lennard-Jones particles (with next-nearest-neighbour interactions to model the stiffness of phantom chains, see section 3.2) one can think of Rouse modes parallel to the elongation as having an increased likelihood of violating the excluded volume constraint between neighbouring monomers. Note that this is a finite-contour length effect and that fluctuations in y- and z-direction are not affected directly. In order to correct for this effect when calculating normal stresses, we determine an effective spring constant $\alpha(\lambda)k_p$ in x-direction. The ratio $\left\langle y_p^2 \right\rangle / \left\langle x_p^2 \right\rangle$ is to a good approximation independent of the mode number p and we determine the correction factor $\alpha(\lambda)$ by averaging this expression over the different modes. Typically, $\alpha(1.5) \approx 1.1$. The normal stresses are then calculated from $\sigma_T = k_p(\alpha \left\langle x_p^2 \right\rangle - \frac{1}{2}(\left\langle y_p^2 \right\rangle + \left\langle z_p^2 \right\rangle))$. The same effects also appear for random and regular IPDN, where we calculate the correction factor $\alpha(\lambda)$ from averages over the modes whose wave lengths are too short to be affected by the tube constraint. In the following, we discuss the long wave length modes in the framework of the CMM.

In agreement with the arguments presented in section 2.4 all mode auto-correlation functions decay to zero for regular IPDN (see Figure 21). For symmetry reasons topological constraints cannot cause finite mean excitations of individual modes. The anticipated reduction of the fluctuations which we have already seen for the Einstein modes is also manifest in the first Rouse mode (table 6). Furthermore, its strain dependence is in qualitative agreement with the CMM: parallel to the elongation the fluctuations are enhanced, while they are reduced in the perpendicular directions.

For random IPDN (table 6, figure 22) the auto-correlation functions of the longest wavelength modes decay to a non-zero $\gamma_p = \lim_{t\to\infty} c_p(t)/c_p(0)$, which is clear evidence for the existence of permanent constraints acting on the chain contours between the cross-links. Closer inspection (figure 17) reveals the existence of a single characteristic length scale beyond which ergodicity is broken by the topological constraints. Our observations agree well with the tube model, which suggests that modes with $p\frac{2N}{N_e} > 1$ can fully relax, while those with longer wave lengths have non-vanishing mean excitations in which elastic energy can be stored. Note that we use a value for the melt entanglement length N_e that was determined from the confinement of the monomer motion in simulations of polymer melts [72]. Under strain, the constrained modes become anisotropic. A quantitative comparison to the CMM (figure 23) will be presented in the discussion.

4.5. Entanglement analysis

In our analysis of the topological constraints we consider only entangled pairs of loops as identified by the Gauß linking number (GLN) $I \neq 0$ (equation (19)). As pointed out by Iwata [12], it is sufficient to consider the smallest loops in the system, since the GLN for larger loops can be written as the sum over contributions from GLNs between the elementary loops. We prepared a list of entanglements by evaluating equation (19) for all pairs of elementary meshes (see section 3.4). Note that the GLN is not defined for pairs of meshes with common monomers and that by considering all $N_{\text{loop}} = N_{\text{strand}}$ different meshes, each bond is used six times. We

Table 7. Linking statistics for meshes in random IPDN. Listed are the number of loops $N_{\rm loop}$, the total number of linked pairs of loops $N_{\rm link}$, the number of links with a GLN larger than one $N_{\rm link}^{|I|>1}$, the number of links between meshes on identical subnets $N_{\rm link}^{\rm intra}$, the radius of gyration of the meshes and the linking radius defined in equation (37).

		$N_{\rm link}$					
N	$N_{\rm loop}$	regular	random	$N_{\rm link}^{\vert I\vert>1}$	$N_{\rm link}^{\rm intra}$	R_g	$R_{\rm L}$
12	640	7680	11120	124	32	4.57±0.03	4.22±0.03
26	896	16128	28508	1478	146	6.74±0.04	6.50±0.03
44	1152	27648	54701	4511	254	8.79±0.06	8.69±0.04

therefore set $\rho_{\rm loop} = \frac{1}{6}N_{\rm loop}/V$ and $\rho_{\rm link} = \frac{1}{36}N_{\rm link}/V$.

The GLN equation (19) is a double integral along the contours of two rings and can be written as a double sum over their bond vectors. The contributions of bond pairs have to be evaluated numerically, possibly using a multi-pol expansion [97]. The direct evaluation of the GLN (equation (19)) for a pair of loops is an order $(6(N+1))^2$ operation and quite time consuming. Instead we first apply a simple reduction operation to the rings [98]: if the triangle defined by any three sequential beads is not crossed by any bond, the middle bead is removed and the outer beads are directly connected. The operation properly maintains the topological state of the two rings but significantly shortens them before equation (19) is evaluated. We have implemented two versions of this operation: one where the criterion is checked exactly using analytical geometry and a faster but cruder method where the loops are projected onto a grid. The latter method has the advantage to be local, i.e. the operations required for on attempted removal of one bead are independent of the ring size. Only in the final phase of the elimination process, when the rings consist of few, relatively long bonds, the geometrical method is more efficient, because the grid algorithm discards too many allowed eliminations. Typically, we were able to reduce the 270×270 bead rings of the $N = 44$ system to 5×5 bead rings before we evaluated the GLN.

Table 7 contains the results of the topological analysis for the regular and the random IPDN. Of the $\frac{1}{2}N_{\rm loop}(N_{\rm loop}-1)$ mesh pairs the GLN identified $N_{\rm link}$ as entangled. The regular IPDN are a convenient test case: In each system we identified the expected number of $3(n-1)$ entanglements per mesh. This confirms, firstly, that during our MD simulations no chain crossings occurred; secondly, that the systems were set up correctly and, thirdly, that our identification of the meshes and of the entanglements between them works correctly.

For the random IPDN the average number $N_{\rm link}/N_{\rm loop}$ of links per loop is higher than the value $n-1$ for regular inter-penetration by a factor of 1.4 ($N = 12$) to 2.0 ($N = 44$). Only $N_{\rm link}^{|I|>1}/N_{\rm link} < 10\%$ of the links have a GLN of 2 or more, demonstrating that for the strand lengths considered simple link topologies dominate and justifying *a posteriori* the use of the Gauss invariant. With $N_{\rm link}^{\rm intra}/N_{\rm link} < 0.5\%$ the number of links between distant neighbour meshes on identical subnets is negligible.† These links are excluded from the subsequent analysis,

† Immediate neighbour meshes are not considered, since the GLN is not defined for pairs of loops that share

since their linking statistics is distorted due to additional interactions within the subnets.

4.6. Linking probabilities

For the analysis of the CM distance dependent linking probabilities $f_N(r)$ we use the data for random IPDN. Thus, we calculate a time average over all mesh pairs that were identified as linked for a *quenched* topology. In principle, the results could be different from an ensemble average over a annealed topology and will be so, for example, in the case of the regular IPDN. However, this procedure should be unproblematic for the quenched *random* topology we consider. Figure 9 illustrates that this is indeed the case for the strand statistics. The reason why we prefer to analyse the data for the quenched system is the great amount of computer time necessary to determine the topology of a single conformation of the networks. In the cases of the phantom or annealed IPDN the topology has to be analysed not just once but for each recorded conformation.

We first determine the characteristic length scale for the entanglement of two loops. Consider an effective linking volume defined as the ratio of the number of entanglements per loop $\frac{N_{\rm link}-N_{\rm link}^{\rm intra}}{N_{\rm loop}}$ and the density of loops belonging to other subnets $\frac{n-1}{n}\frac{N_{\rm loop}}{V}$ in the volume $V=\frac{N_{\rm mon}}{\rho}$. In this case the linking radius is given by

$$R_{\rm L}=\sqrt[3]{\frac{3}{4\pi}\frac{N_{\rm mon}}{\rho}\frac{n}{n-1}\frac{N_{\rm link}-N_{\rm link}^{\rm intra}}{N_{\rm loop}^2}} \tag{37}$$

and of the same order as the mesh radius of gyration. In turn, the latter is almost identical to the bond length of the diamond lattice (table 7). Thus, similarly to the network strands, the extension of the meshes is determined by the lattice structure of the networks and larger than that of free rings with $R_g^2=\frac{1}{2}c_N l^2(N+1)$.

On closer inspection, we observe a small tendency of R_g and $R_{\rm L}$ to grow faster than the pre-set bond length leading to effective exponents of $\nu_g=0.526$ and $\nu_{\rm L}=0.58$. In the case of R_g they can be understood as artifacts due to the chain length dependent stiffness equation (27) of the phantom chains used in the preparation process (for free rings one would observe an exponent of $\nu=0.534$). We will come back to the strong finite-size corrections for the linking radii below.

To obtain the CM distance dependent linking probability $f(r)$ we have calculated pair correlation functions $g_{\rm loop}(r)$ for all loops and $g_{\rm linkedloop}(r)$ for linked loops (figure 18a). To a good approximation the positions of the loops are uncorrelated with $g_{\rm loop}(r)\approx(n-1)/n$ due to the exclusion of loop pairs on identical subnets. The ratio $g_{\rm loop}(r)/g_{\rm linkedloop}(r)$ is the CM distance dependent linking probability $f(r)$.

For regular IPDN (figure 18b) $g_{\rm loop}(r)$ shows strong correlations between the mesh positions. Note, that the typical distance between linked meshes is comparatively small.

Figure 19 shows that the linking probabilities for different chain lengths scale quite well with the linking radius $R_{\rm L}$ (equation (37)) and approximately follow the functional form

$$f_N(\vec{r})\approx\alpha\exp\left(-\frac{\alpha}{2}\frac{r^3}{R_{\rm L}^3}\right)\quad, \tag{38}$$

with $\alpha=0.6$. This ansatz follows from a similar form proposed by Vologodskii *et al* [37, 38]. There is, of course, some uncertainty due to the limited precision of our data for small r where

common strands or cross-links.

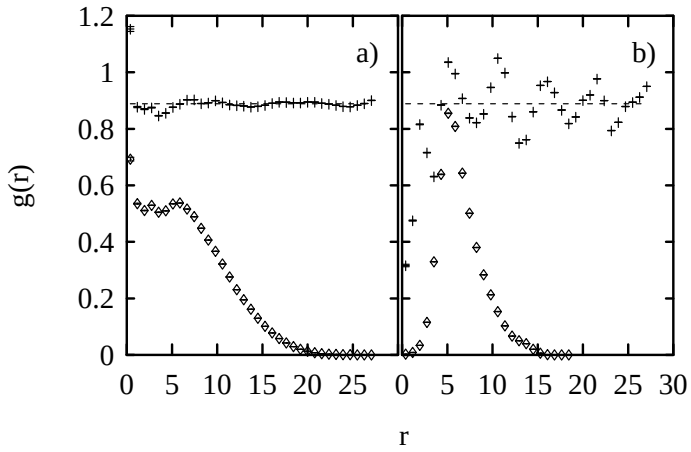

Figure 18. Pair correlation function for the mesh centres of mass for all (+) and for linked ($\diamond$) mesh pairs on different diamond nets with $N = 44$: a) random IPDN, b) regular IPDN. The indicated constant has a value of $\frac{n-1}{n} = \frac{8}{9}$.

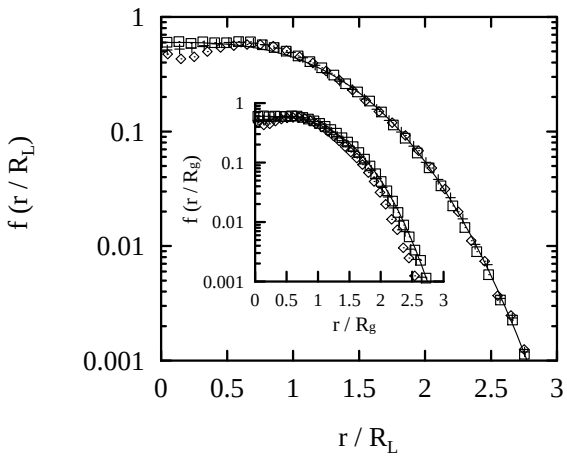

Figure 19. Scaling of the linking probability $f(r)$ for meshes in random IPDN with the linking radius R_{L} defined in equation (37): $N = 44$ (squares), $N = 26$ (+), ($N = 12$) ($\diamond$). The solid line shows the approximate form equation (38). The insert demonstrates that the data do not scale as well with the mesh radius of gyration R_g.

we find only a very week mesh size dependence with $f_N(0) \approx 0.6$. It seems plausible to assume that $\lim_{N\to\infty} f(0) = 1.0$.

These findings can be compared to results of lattice Monte Carlo investigations of the linking properties of closed random walks. Vologodskii *et al* [37, 38] used the Alexander polynomial instead of the GLN and came to very similar conclusions. They observed the weak chain length dependence of $f(0)$ and found—in our notation—an effective exponent $\nu_{\mathrm{L}} = 1.7/3$. The data of Iwata [92] show a more pronounced N-dependence of $f(0)$. When plotted in the manner of figure (19), scaling can also be improved by using an effective exponent larger than 0.5. The existence of pronounced finite-size effects in the linking probabilities of ring polymers is also

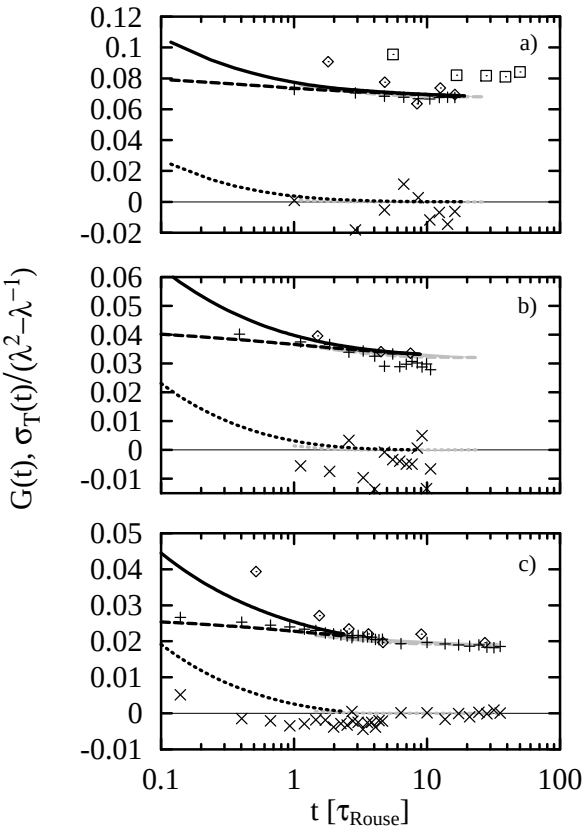

Figure 20. Stress relaxation in phantom (grey) and annealed (black) IPDN after a step strain. The figure shows three different types of data: (i) the suitably normalized measured normal stresses $\sigma_T/(\lambda^2 - 1/\lambda)$ in strained systems for $\lambda = 1.1$ ($\diamond$) and $\lambda = 1.5$ (squares); (ii) normal stresses calculated by applying the Doi-Edwards formula to the stored network conformations for the strained systems ($*$) and the separation of this result into a classical ($+$) and a tube ($\times$) contribution; (iii) estimates for the shear relaxation modulus $G(t)$ from the CMM equation (13) and an analysis of the fluctuations in the *unstrained* networks (——), again split into a classical (– – –) and a tube contribution ($\cdots$).

confirmed in a recent study for walks on a lattice with better statistics [50]. All in all, our findings are good agreement with studies of ring polymers and we observe no serious artifacts due to the investigation of mesh pairs in spanned networks.

5. Discussion

After having shown that our model networks display a purely entropic elasticity and equipped with the detailed microscopic information presented in the previous section we are now in a position to quantitatively test the theoretical approaches to the physics of rubber elasticity presented in section 2. In principle, we can directly compare their *parameter-free* predictions for the shear modulus and the deformation of the network strands to our observations. In particular, we do not rely on an extrapolation of our results to the limit of infinite strand length, but quantify

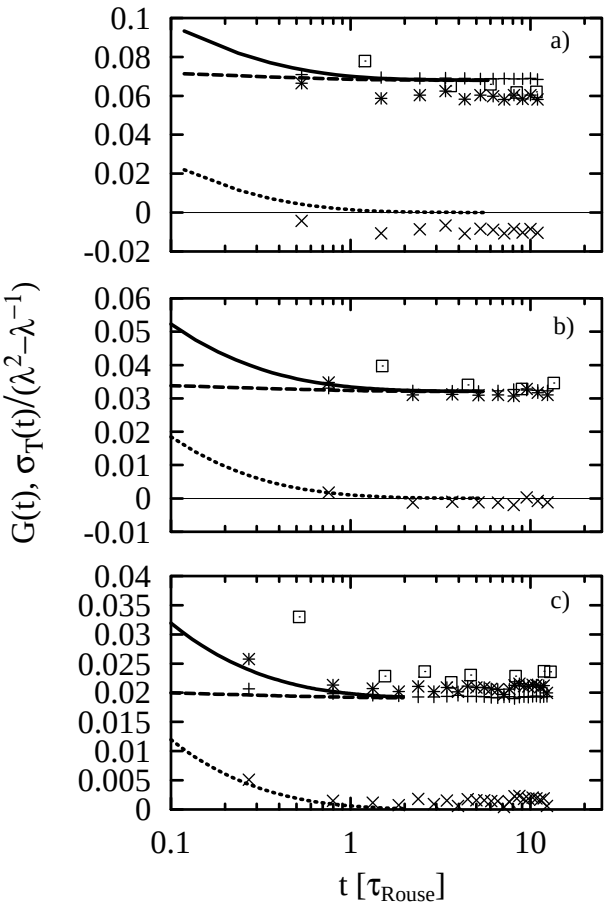

Figure 21. Shear relaxation modulus for regular IPDN. For an explanation see figure 20.

the effects directly for the systems under consideration.

In practice, we are somewhat limited by the quality of our data even though the total numerical effort corresponds to some 1000 hours on a Cray Y/MP. Our limited resources of computer time did, for example, preclude the calculation of many data points on the stress–strain curves and the investigation of several random IPDN with *different* quenched disorder. A comparison of the two random IPDN with $N = 12$ indicates, however, that self-averaging is not critical.

Polymer networks are very soft systems and in order to provoke measurable effects we had to introduce strains of the order of 50%. While such deformations are also typically used in experiments, they exceed by far the validity range of linear response. Instead, we extract the shear moduli by assuming the neo-Hookean behaviour, $\sigma_T = G(\lambda^2 - 1/\lambda)$. Typically, this ansatz tends to *underestimate* the shear moduli, even though a rough, *a posteriori* consistency check based on the CMM suggests that the deviations are smaller than the margins of error cited in table 8. For future investigations it would be interesting to reconsider the fluctuations formalism employed by Barsky *et al* [99, 100], which might give better results for networks beyond the vulcanization threshold.

In some cases, one can avoid the problems associated with the extrapolation of data to zero

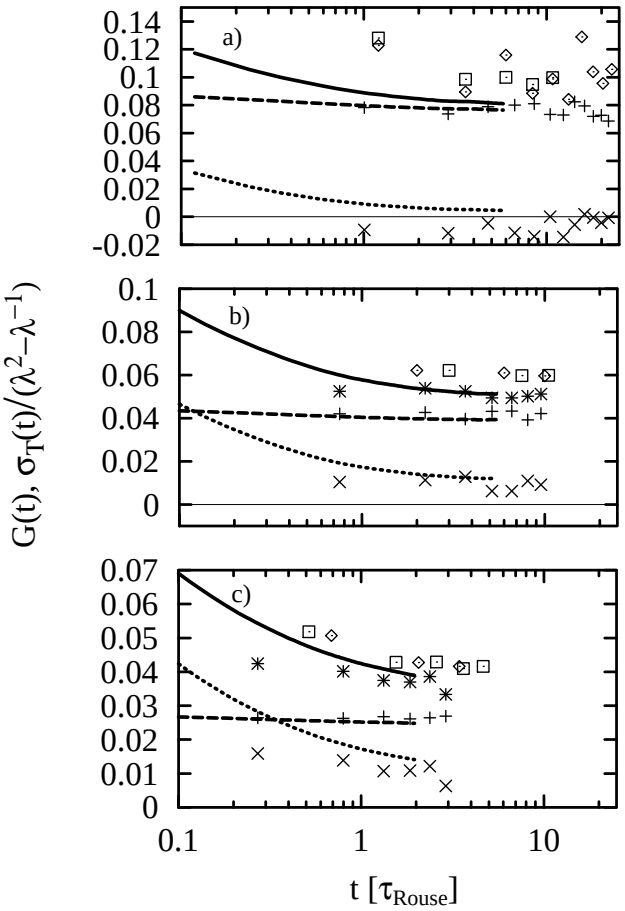

Figure 22. Shear relaxation modulus for random IPDN. For an explanation see figure 20.

strain by comparing measured and theoretically expected normal tensions for a given system at finite strain. The latter are obtained within a model from the stored conformations of the network. For example, one can test the classical models by calculating the normal stresses for an appropriate ensemble of independent entropic springs which have the observed strand elongations. Unfortunately, this approach raises a different kind of problem when extended to the Rouse modes as our model polymers are (as real polymers) not truly Gaussian chains. Such finite chain length effects may be cumbersome for a test of theories which treat the polymers as Gaussian, but they also give a hint to what kind of complications may arise in experimental systems.

5.1. Classical rubber elasticity

The classical theories (section 2.5) are based on the assumption that the elastic response of rubber has its sole origin in the elongation of the network strands. Two question are of principal interest:

(i) In a *strained* sample, do the measured normal stresses agree with those calculated within the classical approximation from the elongation of the network strands?

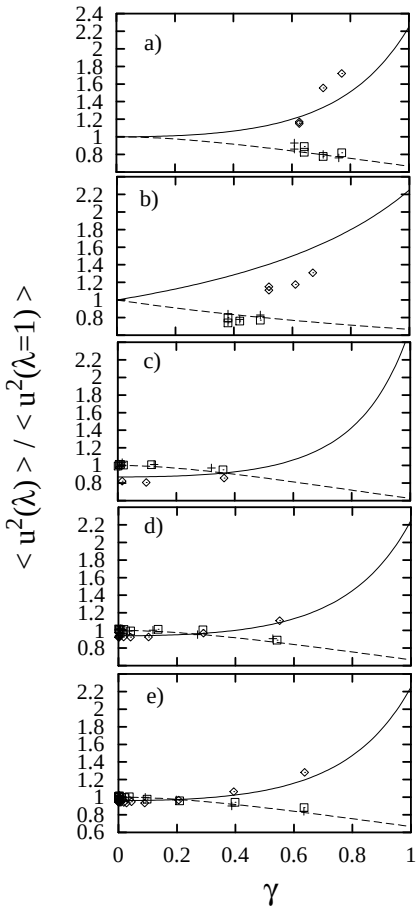

Figure 23. Excitation of partially confined modes in strained networks and the predictions of the CMM parallel (◇, ——) and perpendicular (+,squares,– – –) to the elongation. (a) Flory–Einstein modes in random IPDN for $N = 12, 26, 44$ from left to right; (b) Flory–Einstein modes in regular IPDN for $N = 12, 26, 44$ from left to right; (c) Rouse modes in random IPDN for $N = 12$; (d) Rouse modes in random IPDN for $N = 26$; (e) Rouse modes in random IPDN for $N = 44$.

(ii) Can the latter be predicted from a constrained junction model and an analysis of the fluctuations in the *unstrained* state?

In short, the answers to these two questions are no and yes respectively. In Figures 20 to 22 we compare the normal stresses measured during the relaxation of the strained networks (squares, diamonds) to the classical normal stresses in the corresponding system of entropic springs using the stored cross-link positions (+) and the predictions of the CMM based on the analysis of the fluctuations and average extensions of the network strands in the *unstrained* samples. While the agreement is excellent for the phantom and annealed IPDN, there is a clear discrepancy between the actual and the classical normal stress in the case of the random IPDN which increases with the strand length. Nevertheless, the classical contribution to the normal stress is well predicted by the CMM.

We are primarily interested in the asymptotic normal stresses for long times. They can be obtained from the strand end-to-end distance distributions in the strained networks using

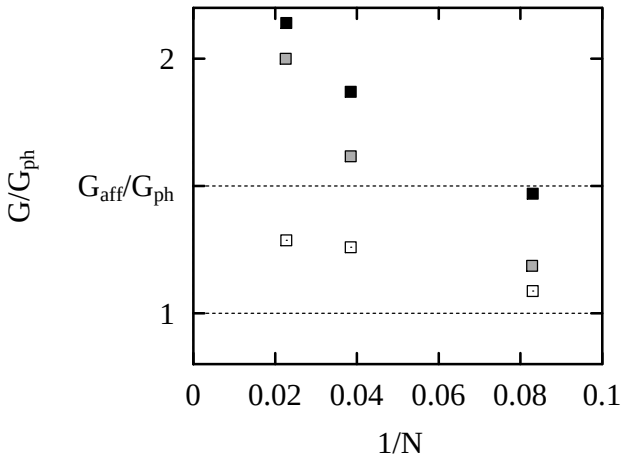

Figure 24. Strand length dependence of the shear modulus: measured values (black), classical (white) and the sum (grey) of classical and tube contribution. For simplicity we used the approximate expressions in equations (8) and (14) for the normalization.

equation (7), the values listed in tables 4 and 5 and

$$\sigma_T^{\text{class}}(\vec{R}_\lambda, \vec{\Delta}_\lambda) = \frac{3k_\text{B}T}{R^2}\rho_{\text{strand}}\left(X_\lambda^2 - \frac{1}{2}\left(Y_\lambda^2 + Z_\lambda^2\right) + (\Delta_\lambda^x)^2 - \frac{1}{2}\left((\Delta_\lambda^y)^2 + (\Delta_\lambda^z)^2\right)\right) \tag{39}$$

$$G_{\text{class}} \approx \frac{\sigma_T^{\text{class}}(\lambda)}{\lambda^2 - \lambda^{-1}} \quad . \tag{40}$$

The resulting estimate for the classical modulus has therefore two terms corresponding to the changes in the mean extensions, $\vec{R}_\lambda$, and in the width of the fluctuation, $\vec{\Delta}_\lambda$. The value for G_{class} obtained in this way contains a small approximation as we assume the validity of the ideal stress–strain relation. This ansatz has, however, the advantage of being consistent with the way we estimated the true moduli. For the results listed in table 8 we used the calculated stiffness equation (27) for the phantom IPDN and $c_N = 1.7$ in all other cases.

For phantom and annealed IPDN calculated and measured values are in excellent agreement. The small fluctuation contribution for phantom IPDN with $N = 12$ is probably a finite strand length effect similar to those discussed in section 4.4 and should be ignored. In the case of the annealed IPDN the remaining fluctuation contributions reflect the long relaxation times (see figure 12) and explain why the measured moduli slightly exceed the phantom network values.

The deviation of the classical from the observed normal stresses in the random IPDN is illustrated in figure 24. The shear moduli from table 8 are normalized to the predictions of the phantom model and the horizontal line at $G_{\text{aff}}/G_{\text{ph}} = 3/2$ indicates the upper limit for the classical theories of rubber elasticity.† The true moduli are beyond the predictions of the affine model and increasingly exceed the classical predictions. This shows that *it is not*

† Please recall that this unusual ratio is due to the pre-stretching of the strands in the diamond nets. For a randomly cross-linked melt with four-functional cross-links the predictions of the affine and the phantom model differ by a factor of 2.

Table 8. Measured (G), classical ($G_{\rm class}$) and tube ($G_{\rm tube}$) shear moduli for IPDN and the ration $(G - G_{\rm ph})/\rho_{\rm link}$ of the entanglement contribution to the shear modulus and the density of topological links between meshes. The measured values, G, were derived from the normal stresses observed in simulations of strained networks. The classical shear moduli were calculated from equation (40) and the contributions due to the changes in the peak positions and the widths of the end-to-end distance distributions are listed separately. We estimate the errors in the estimates for $G_{\rm class}$ to be of the order of $\pm 0.001\epsilon/\sigma^3$ and about twice that value for $G_{\rm tube}$.

System	G N	$G_{\rm class}$ $[\epsilon/\sigma^3]$	$G_{\rm tube}$ $[\epsilon/\sigma^3]$	$\frac{G-G_{\rm ph}}{\rho_{\rm link}}$ $[\epsilon/\sigma^3]$	$[\epsilon]$
	12	0.083 ± 0.002	$0.080(-0.003)$		
Phantom	26	—	—		
IPDN	44	0.020 ± 0.002	0.019		
	12	0.071 ± 0.003	0.071		
Annealed	26	0.035 ± 0.003	0.032		
IPDN	44	0.021 ± 0.003	$0.019(+0.002)$		
	12	0.100 ± 0.003	$0.075 + 0.005$	0.004	0.85
Random	26	0.060 ± 0.003	$0.034 + 0.007$	0.009	0.88
IPDN	44	0.041 ± 0.002	$0.019 + 0.006$	0.009	0.83
	12	0.071 ± 0.003	$0.072 + 0.003$	0.000	0.0
Regular	26	0.034 ± 0.003	$0.032 + 0.002$	0.002	0.0
IPDN	44	0.025 ± 0.003	$0.019 + 0.001$	0.003	0.31

possible to calculate the topology contribution to the modulus from the constraints on the junction fluctuations alone.

Nevertheless, the comparison in figure 22 shows that the constrained junction model does very well in predicting the classical contribution to the normal stress. This contribution is, however, dominated by the (trivial) phantom model stress and a more detailed test has to address the deformation dependence of the fluctuations of strand extensions. In figure 23(a) we plot the observed values for the parallel and perpendicular fluctuations in strained systems versus the degree of confinement, γ, in comparison to the predictions of the CMM. Measuring these quantities with high precision requires much longer simulations than we were able to perform. Incomplete relaxation of the network conformations would tend to increase the values, so that we consider the agreement with the theoretical curves as satisfactory.

The case of the regular IPDN is quite difficult to handle as the observed effects are of the order of our margins of error. In the strained system the measured normal stresses are very similar to those for phantom networks, which comes as a surprise for systems with permanent topological constraints. Regarding a test of the CMM one has to take into account that fluctuations are confined in different ways in systems with quenched *regular* and quenched *random* topology (section 2.4). For example, the CMM shear relaxation moduli in figure 21 have to be taken with a grain of salt, since we calculated them for comparison with the other cases from the mode

auto-correlation functions and equation (13). Nevertheless, some observations can be made which confirm, at least qualitatively, the picture suggested by the CMM. We note first that the anisotropy of the fluctuations of the strand elongations for $\lambda = 1.0$ (tables 5) explains the small negative normal stresses we observed in these systems (the estimates for the moduli are always calculated from the difference $\sigma_T(\lambda) - \sigma_T(1.0)$). Another curiosity is that the Einstein modes do not contribute to the normal tensions in figure 21, since they happen to become *isotropic* for elongations around $\lambda = 1.5$ (table 5). The classical normal tensions are therefore just those expected for a phantom network.

5.2. The tube model

The results presented in the preceding section indicate that the constrained junction models are capable of predicting the classical contribution to the normal stresses in a strained polymer network, but that they miss important contributions to the elastic response. The question then arises whether this deficiency can be remedied within a single-chain theory. The tube model suggests that the classical approach fails to account for constraints acting on the network strands *between* the cross-links. Even though there is convincing evidence from simulations [72, 75] as well as from SANS experiments [70] for the existence of the tube, it is less clear that these effects can account for the total elastic response. The situation could be analogous to the case of the constrained junction models, which we had to reject even though we confirmed the underlying microscopic picture. Thus, the idea that an entangled network can be represented as an ensemble of effectively constrained, single chains can (and must) be tested independently of the tube model. We will nevertheless be somewhat relaxed in our terminology and refer to the part of the shear modulus due to the constraints along the strand contours as the 'tube contribution', G_{tube}.

Again the problem separates into several independent parts:

(i) Is there an effect of topological constraints on the fluctuations of the network strands *between* the cross-links?

(ii) Is this effect of the form predicted by the tube model?

(iii) In a strained sample, do the measured normal stresses agree with those obtained by applying the Doi–Edwards formula to the observed *conformations* (and not just *elongations*) of the network strands?

(iv) Can the latter be predicted from, for example, the constrained mode model and an analysis of the fluctuations in the unstrained state?

Concerning the first point, our analysis of the single chain Rouse modes in section 4.4 confirms the existence of such an effect in our model networks. In regular IPDN the topological constraints suppress the fluctuations compared to the other cases, in random IPDN the non-decaying mode auto-correlation functions indicate the finite mean-excitations of individual modes. Figure 17 shows that independent of strand length only modes with a wavelength larger than a certain characteristic length are affected. Furthermore, the extrapolation of the measured moduli to infinite strand length (section 4.2, figure 8) agrees well with an estimate of the plateau modulus based on the chain dynamics in entangled polymer melts. While this supports the tube model, we emphasize that the second point is more suitably addressed in simulations of randomly end-linked melts with strand length $N \gg N_{\mathrm{e}}$ [75].

Similarly to Gao and Weiner [86], who investigated the relaxation of stress in simulations of entangled polymer melts, we find reasonable agreement between the measured normal stresses

and the single chain tensions calculated from the stored conformations of the relaxing, strained random IPDN. Figure 22 shows the sum (marked by $*$) of the tube contribution ($\times$) and the classical contribution discussed in the previous section. Considering that this comparison is (i) based on an enormous simplification (an ensemble of single chains at the place of an entangled network) and (ii) contains only a single, *not* adjustable parameter (the size $\langle r^2 \rangle$ of the free strand in a melt), the agreement is remarkable. On the other hand, the agreement is not perfect. The entropic normal stresses underestimate the true values by an amount comparable to our estimates of the entanglement contributions. What complicates the comparison are the finite strand length effects discussed in section 4.4 which lead to anisotropic fluctuations in elongated network strands. While we have tried to correct for this effect, there remains some uncertainty in the value of the tube contribution to the normal stress for the shorter strand length. The negative values in figures 20 to 22 give an impression of the magnitude of the problem. We have, however, deliberately not pushed the analysis any further as this risks over-interpreting the data. In view of the considerable theoretical implications [42], it would be very interesting to repeat the test of the exactness of the Doi–Edwards stress formula with better data for longer chains.

Regarding the fourth point, Figure 22 shows that there is nice agreement between the prediction of the CMM and (with the reservations just made) the observed stresses in strained random IPDN.† Quite interestingly, the mode analysis yields an almost strand length independent value for G_{tube}, reminiscent of the experimentally observed plateau modulus. The deformation dependence of the excitation of the strand modes constitutes a more detailed test of the CMM. In figure 23c-e we plot the observed values for the parallel and perpendicular fluctuations, $\left\langle u_p^2 \right\rangle (\lambda = 1.5)$, in strained systems normalized to $\left\langle u_p^2 \right\rangle (\lambda = 1)$ versus the degree of confinement, γ. The fact that these ratios hardly deviate from one even for modes experiencing a considerable confinement is a clear indication for the deformation dependence of the confining potentials. Again the results are affected by the deviations from the Gaussian behaviour. Correcting the theoretical predictions of the CMM for this, the agreement is quite good.

In the case of the regular IPDN the difficulties mentioned in the previous section apply even more to the analysis of the confinement of the strands between the cross-links. What seems to be clear is that (i) for the range of strand lengths studied only the first strand mode is affected by topological constraints, that (ii) there is at least for $N = 44$ a small contribution of this first mode to the normal stresses in the strained system, and that (iii) this can at least be understood qualitatively by taking into account the different ways in which fluctuations are confined in systems with quenched *regular* and quenched *random* topology.

5.3. The topological approach

In the previous sections we have shown that the combined effect of many entanglements can be well understood from an analysis of the reduced fluctuations of the network strands. However, the *strength* of this effect is characterized purely phenomenologically by the entanglement length, N_{e}. In the present section we address the complementary topological theories of rubber

† Note that the shear moduli calculated from the formula used by Duering *et al* [75] clearly overestimate the effect. For example, this analysis yields for the case of $N = 44$ a tube contribution to the shear modulus equal to the classical contribution, while figure 22 shows that the strand modes account only for one third of the normal stress. Nevertheless, even if the results obtained for randomly cross- and end-linked melts are too high by 30%, the error should become *independent* of strand length for $N \gg N_{\mathrm{e}}$ and does not invalidate qualitatively the conclusions drawn by the authors.

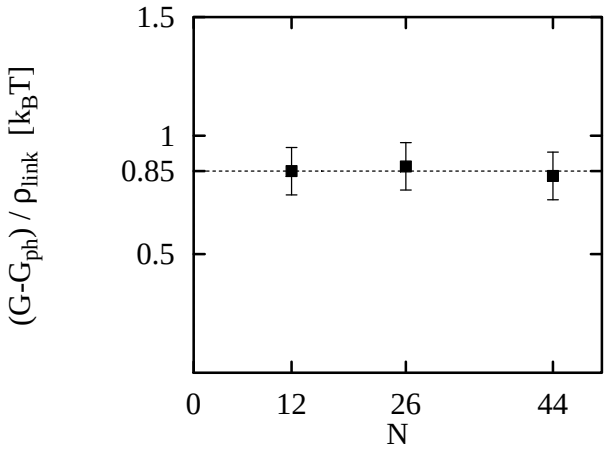

Figure 25. Strand length dependence of the ratio of the topology contribution $G - G_{\rm ph}$ to the modulus and the entanglement density $\rho_{\rm link}$.

elasticity and the question, whether it is possible to estimate the entanglement contribution to the shear modulus from an entropic interaction between pairs of entangled loops. The model of Graessley and Pearson (GP) [11] is particularly transparent; other, mathematically more involved theories [12, 13] are based on the same physical ideas.

A key prediction, which can be derived from the GP theory, is the proportionality of the entanglement contribution to the shear modulus, $G - G_{\rm ph}$, and the density of topological links, $\rho_{\rm links}$, between mesh pairs (equation (21)). The details of the topological interactions only enter the prefactor (equation (22)). Clearly, there is no point in elaborating this approach if the proposed proportionality between cause and effect does not hold. While it is difficult to envision an experimental test, we can directly compare our results for the shear moduli and and the linking density (table 8).

Figure 25 shows that for the strand lengths investigated (the mesh size $6(N+1)$ varies between 2 and 8 $N_{\rm e}$) one indeed observes $G - G_{\rm ph} = 0.85\,\rho_{\rm links}\,k_{\rm B}T$ for the random IPDN. This is a strong hint that (i) loop entanglements contribute to the elastic response in the manner suggested by Vologodskii *et al* [37, 38] and Graessley and Pearson [11] and (ii) that they do so dominantly compared to higher order topological interactions.

The second step in the analysis is to check that the GP estimate of the proportionality factor $a[f(r)]$ is consistent with the observed value $0.85k_{\rm B}T$. Using our result for the linking probability $f(r)$ from section 4.6 and evaluating equation(22) numerically, we obtain the absolute, *parameter-free* prediction of the GP model $\frac{G_{\rm link}}{\rho_{\rm link}} = a[f(x)] = 1.3\,k_{\rm B}T$, which agrees with the measured value up to a numerical constant $a_0 = (G - G_{\rm ph})/G_{\rm link} \approx 2/3$ of order one. Considering the crudeness of the GP model this is a remarkable success. Asymptotically, however, this simple entanglement definition has to break down: $G_{\rm link} \sim \rho_{\rm link} \sim \rho_{\rm loop}^2 R_{\rm L}^3 \sim N^{-0.5}$ vanishes and cannot explain an asymptotic shear modulus of the order of the melt plateau modulus. Since we have first indications that a refined analysis of more complicated two loop interactions does not fundamentally alter this picture [50], it might be necessary to study higher-order interactions between three or more rings.

While the GP theory thus seems to work quite well for random IPDN, it cannot provide a quantitative explanation for the apparent ineffectiveness of the entanglements in regular IPDN.

The link densities are at most a factor of two smaller than in the random case (section 4.5), while there are no significant entanglement contributions to the shear modulus (table 8). Within the GP model, one can argue [97] that the smaller average CM distance of the linked meshes in regular IPDN makes them less effective for the modulus. The calculated reduction is, however, too small to explain the observed effect. This failure is not too surprising, since one of the major assumptions of the GP model is not valid in these systems: the entanglements between different diamond networks are not random but highly correlated. Some insight can be gained by noting that the comparable entanglement densities in random and regular IPDNs lead to comparable *degrees of confinement* for the fluctuations. Why the resulting entanglement contributions to the shear modulus are so different, is then explained by the CMM.

5.4. Outlook

While diamond networks are a useful model system for some fundamental aspects of the entanglement problem, it would be very interesting to extend the present analysis to more realistic network architectures such as end-linked melts and, in particular, to systems with strand lengths $N \gg N_e$. Also, while the CMM has some merits for a test of the ideas underlying the constrained fluctuation theories of rubber elasticity and the analysis of simulation data, other theories might be more useful in the absence of such detailed information. For example, it is difficult to predict the macroscopic behaviour of a network without a better understanding of how the crossover of the confinement parameters γ_p from zero to one occurs for modes of different wavelength. Moreover, the CMM makes a fairly drastic approximation in treating the Einstein and Rouse modes as eigenmodes of the entangled network. It would therefore be interesting to test other theories, which are based on slightly different (but equally drastic) approximations. Obvious candidates are the tube model of Straube *et al* [27], which has recently been used with great success to explain SANS data for strained, entangled networks [70], and the model by Rubinstein and Panyukov [41] which, as the CMM, attempts a synthesis of the constrained junction and the tube model. An important criterion should be the simultaneous prediction of the conformations (as they are indirectly seen in SANS experiments) and the elastic response. In view of the profound implications for the modeling of the confinement [42], some attention should be given to possible deviations from the Doi–Edwards formula for the normal stress.

6. Summary

In this paper we have presented a detailed account of molecular dynamics simulations of interpenetrating polymer networks with diamond lattice connectivity (IPDN). The idea was to test the predictions of different statistical mechanical models of rubber elasticity by making extensive use of the microscopic structural, dynamic and topological information available in computer simulations.

The IPDN were designed as highly idealized model systems which isolate the effect of topology conservation from other sources of quenched disorder. By varying the interaction potentials and the mode of preparation we have studied four different types of IPDN: (i) (almost) trivial *phantom* IPDN as a reference case and for the preparation of equilibrated initial conformations for the other types, (ii) *annealed* IPDN where softened excluded volume interactions lead to the typical monomer packing in a melt *without* rendering the chains mutually impenetrable, (iii) *random* IPDN of the usual Kremer–Grest polymer model with quenched

random topology, and (iv) *regular* IPDN with the conserved regular topology of intercalating diamond lattices. The investigated strand lengths were $N = 12, 26, 44$ compared to $N_e = 35$ in the Kremer–Grest model. All systems were studied in the unstrained state of preparation as well as after a volume conserving, uni-directional elongation of typically 50%.

By measuring normal stresses and internal energies under strain we were able to measure the macroscopic shear moduli of all systems and to show that they exhibit a purely entropic elasticity. For annealed IPDN the shear moduli agree with the predictions of the phantom model, showing that excluded volume interactions as such do not contribute to the elastic response. For random IPDN the observed values were up to twice as large, thus we quantitatively observe a significant entanglement contribution to the shear modulus. The measured values support the tube model and are in contradiction to the classical theories, because they (i) exceed the prediction of the junction affine model and (ii) extrapolate to a finite value of the order $\rho k_B T/N_e$ in the limit of infinite strand length.

We have analysed the entanglement effects on the microscopic dynamics and deformations in the framework of the constrained mode model [42]. The CMM casts the ideas of Flory [20] and Edwards [24] into a form which is particularly suited for the analysis of simulation data. Treating the motion of cross-links and networks strands as independent Einstein and Rouse modes respectively, one can directly distinguish the two types of entanglement effects discussed in the constrained junction and the tube model.

The Einstein modes are most strongly affected by the entanglements and clearly show the behaviour anticipated by the constrained junction models: (i) Individual modes exhibit reduced fluctuations around non-vanishing mean values. (ii) The ensemble averages are nevertheless identical for unstrained phantom, annealed, and random IPDN, since in systems with *randomly* quenched topology entanglements do not affect the statics in the state of preparation. † (iii) In stretched samples, constrained modes become anisotropic and the strength of the confinement is reduced parallel and increased perpendicular to the axes of elongation. (iv) The strength of the confinement increases with the strand length.

However, contrary to the assumptions of the classical models, we clearly observe tube effects even for our comparatively short network strands. For long wavelength Rouse modes we find qualitatively the same behaviour as for the Einstein modes and comparable degrees of confinement. Only Rouse modes with wavelengths significantly shorter than the melt entanglement length, N_e, are not affected by the topological constraints.

The quantitative success of the CMM in *predicting* the chain conformations under strain from an analysis of the confined fluctuations in the unstrained networks strongly supports the idea underlying all constrained fluctuation theories of rubber elasticity. Given the microscopic conformations under strain, the evaluation of the Doi–Edwards expression yields reasonable normal stresses, *provided* the tube contribution from the partially constrained Rouse modes is taken into account. Our results immediately prove that the omission of this term in the classical theories leads to a systematic error which does *not* have the form of a more or less uncritical prefactor as it was suggested in the long debates on the front-factor problem. The observed tube contribution is independent of strand length and, in agreement with the extrapolation of the macroscopic shear moduli, is bound to dominate the elastic response for systems with $N \gg N_e$. We therefore strongly reject conclusions drawn, for example, by Erman and Flory [58] from

† In regular IPDN, on the other hand, the confinement is identical for all strands leading to reduced fluctuations which, for symmetry reasons, are centred around zero.

successful fitting of stress–strain curves that the constraints on the chain contours make no 'appreciable contribution' to the elastic properties of polymer networks.

Finally, we have presented a first quantitative test of a *topological* theory of rubber elasticity, the second theoretical approach initiated by Edwards almost thirty years ago [7, 8]. We find that for the comparatively short strand lengths in our simulations the topology contribution to the elastic response is proportional to the density of entangled mesh pairs with non-zero Gauss linking number. Moreover, the prefactor can be estimated consistently within a rather simple model developed by Vologodskii *et al* [37, 38] and by Graessley and Pearson [11], which is based on the definition of an entropic interaction between the centres of mass of two loops in a conserved topological state. Although encouraging, it is far from obvious how this result could be generalized to an explanation of the tube model. However, whatever the possible answers, we are convinced that their test requires investigations along the lines of this paper.

Acknowledgements

The molecular dynamics simulations presented in this paper and the initial data analysis were part of my PhD work and carried out in close collaboration with my supervisor, K Kremer, to whom, along with G S Grest and M Pütz I am also greatly indebted for many subsequent discussions. This work was supported by a generous CPU time grant from the German Supercomputer Center HLRZ (Jülich) within the Disordered Polymer Project.

References

[1] Treloar L R G 1975 *The Physics of Rubber Elasticity* (Oxford: Clarendon)
[2] Deam R T and Edwards S F 1976 *Phil. Trans. R. Soc.* A **280** 317
[3] Mezard M, Parisi G and Virasoro M V 1987 *Spinglas Theory and Beyond* (Singapore: World Scientific)
[4] James H 1947 *J. Chem. Phys.* **15** 651
[5] James H and Guth E 1947 *J. Chem. Phys.* **15** 669
[6] Flory P J 1976 *Proc. R. Soc.* A **351** 351
[7] Edwards S F 1967 *Proc. Phys. Soc.* **91** 513
[8] Edwards S F 1968 *J. Phys. A: Gen. Phys.* **1** 15
[9] Rolfsen D 1996 *Knots and Links* (Berkeley, CA: Publish or Perish)
[10] Prager S and Frisch H L 1967 *J. Chem. Phys.* **46** 1475
[11] Graessley W W and Pearson D S 1977 *J. Chem. Phys.* **66** 3363
[12] Iwata K 1982 *J. Chem. Phys.* **76** 6363
[13] Iwata K 1985 *J. Chem. Phys.* **83** 1969
[14] Brereton M G and Filbrandt M 1986 *Polymer* **26** 1134
[15] Iwata K and Edwards S F 1989 *J. Chem. Phys.* **90** 4567
[16] Otto M and Vilgis T A 1997 *Phys. Rev.* E **56** R1314
[17] Vilgis T A and Otto M 1998 *Phys. Rev. Lett.* **80** 881
[18] Müller-Needebock K K and Edwards S F 1999 *J. Phys. A: Math. Gen.* **32** 3301
[19] Ronca G and Allegra G 1975 *J. Chem. Phys.* **63** 4990
[20] Flory P J 1977 *J. Chem. Phys.* **66** 5720
[21] Erman B and Flory P J 1978 *J. Chem. Phys.* **68** 5363
[22] Flory P J and Erman B 1982 *Macromol.* **15** 800
[23] Kästner S 1981 *Colloid Polymer Sci.* **259** 499, 508
[24] Edwards S F 1967 *Proc. Phys. Soc.* **92** 9

[25] Doi M and Edwards S F 1986 *The Theory of Polymer Dynamics* (Oxford: Claredon)
[26] Graessley W W 1982 *Adv. Pol. Sci.* **47** 67
[27] Heinrich G, Straube E and Helmis G 1988 *Adv. Pol. Sci.* **85** 34
[28] Edwards S F and Vilgis T A 1988 *Rep. Prog. Phys.* **51** 243
[29] Flory P J 1949 *J. Chem. Phys.* **17** 303
[30] Panyukov S and Rabin Y 1996 *Phys. Rep.* **269** 1
[31] Goldbart P, Castello H E and Zippelius A 1996 *Adv. Mod. Phys.* **45** 393
[32] Higgs P G and Ball R C 1988 *J. Physique* **49** 1785
[33] Solf M P and Vilgis T A 1995 *J. Phys. A: Math. Gen.* **28** 6655
[34] Solf M P and Vilgis T A 1996 *J. Physique* I **6** 1451
[35] White J 1989 *Mathematical Methods in DNA Sequencing* ed S Wassermann (Boca Raton, FL: CRC Press)
[36] Langley N R 1968 *Macromol.* **1** 348
[37] Vologodskii A V, Lukashin A V and Frank-Kamenetskii M D 1975 *Sov. Phys.–JETP* **40** 932
[38] Frank-Kamenetskii M D, Lukashin A V and Vologodskii A V 1975 *Nature* **258** 398
[39] Marrucci G 1981 *Macromol.* **14** 434
[40] Gaylord R J 1982 *J. Polymer Bull.* **8** 325
[41] Rubinstein M and Panyukov S 1997 *Macromol.* **30** 8036
[42] Everaers R 1998 *Eur. J. Phys.* B **4** 341
[43] Ball R C, Doi M, Edwards S F and Warner M 1981 *Polymer* **22** 1010
[44] Edwards S F and Vilgis T A 1986 *Polymer* **27** 483
[45] Adolf D 1988 *Macromol.* **21** 228
[46] Kosc M 1988 *Colloid Polymmer Sci.* **266** 105
[47] Higgs P G and Ball R C 1989 *Europhys. Lett.* **8** 357
[48] de Gennes P G 1971 *J. Chem. Phys.* **55** 572
[49] Everaers R and Kremer K 1996 *Phys. Rev.* E **53** R37
[50] Auhl R, Everaers R and Kremer K, in preparation
[51] Moore C G and Watson W F 1956 *J. Polymer Sci.* **19** 237
[52] Mullins L 1959 *J. Appl. Polymer Sci.* **2** 1
[53] Pearson D S and Graessley W W 1980 *Macromol.* **13** 1001
[54] Gottlieb M *et al* 1981 *Macromol.* **14** 1039
[55] Gottlieb M and Gaylord R J 1983 *Polymer* **24** 1644
[56] Gottlieb M and Gaylord R J 1984 *Macromol.* **17** 2024
[57] Gottlieb M and Gaylord R J 1987 *Macromol.* **20** 130
[58] Erman B and Flory P J 1982 *Macromol.* **15** 806
[59] Mark J E 1982 *Adv. Pol. Sci.* **44** 1
[60] Queslel J P and Mark J E 1984 *Adv. Pol. Sci.* **65** 135
[61] Opperman W and Rennar N 1987 *Prog. Colloid Polymer Sci.* **75** 49
[62] Patel S K, Malone S, Cohen C and Gillmor J R 1992 *Macromol.* **25** 5241
[63] Sharaf M A and Mark J E 1994 *Polymer* **35** 740
[64] Hild G 1998 *Prog. Polymer Sci.* **23** 1019
[65] Higgs P G and Gaylord R J 1990 *Polymer* **31** 70
[66] Vilgis T A and Erman B 1993 *Macromol.* **26** 6657
[67] Grest G S, Kremer K and Duering E R 1992 *Europhys. Lett.* **19** 195
[68] Richter D *et al* 1990 *Phys. Rev. Lett.* **64** 1389
[69] Richter D *et al* 1993 *Phys. Rev. Lett.* **71** 4158
[70] Straube E *et al* 1995 *Phys. Rev. Lett.* **74** 4464
[71] Kremer K and Grest G S 1995 *Monte Carlo and Molecular Dynamics Simulations in Polymer Science* ed K Binder (Oxford: Oxford University Press)
[72] Kremer K and Grest G S 1990 *J. Chem. Phys.* **92** 5057

[73] Paul W, Binder K, Heermann D W and Kremer K 1991 *J. Chem. Phys.* **95** 7726
[74] Grest G S, Kremer K and Duering E R 1993 *Physica* A **194** 330
[75] Duering E R, Kremer K and Grest G S 1994 *J. Chem. Phys.* **101** 8169
[76] Duering E R, Kremer K and Grest G S 1991 *Phys. Rev. Lett.* **67** 3531
[77] Duering E R, Kremer K and Grest G S *Macromol.* **26** 3241
[78] Everaers R and Kremer K 1995 *Macromol.* **28** 7291
[79] Everaers R, Kremer K and Grest G S 1995 *Macromol. Symposia* **93** 53
[80] Everaers R and Kremer K 1996 *J. Mol. Mod.* **2** 293
[81] Flory P J and Rehner J 1943 *J. Chem. Phys.* **11** 512
[82] Everaers R and Kremer K 1999 *Anomalous Diffusion: From Basis to Applications* ed R Kutner and A Pękalski (Heidelberg: Springer) in press
[83] Duiser J A and Stavermann A J 1965 *Physics of Non-Crystalline Solids* ed J Prins (Amsterdam: North-Holland) p 376
[84] Eichinger B E 1972 *Macromol.* **5** 496
[85] Graessley W W 1975 *Macromol.* **8** 186, 865
[86] Gao J and Weiner J H 1995 *J. Chem. Phys.* **103** 1614
[87] Wiegel F W 1986 *Introduction to Path Integral Methods in Physics and Polymer Science* (Philadelphia, PA: World Scientific)
[88] Orlandini E, van Rensburg E J J, Tesi M C and Whittington S G 1994 *J. Phys. A: Math. Gen.* **27** 335
[89] Iwata K and Kimura T 1981 *J. Chem. Phys.* **74** 2039
[90] Tanaka F 1982 *Prog. Theor. Phys.* **68** 148
[91] Tanaka F 1982 *Prog. Theor. Phys.* **68** 164
[92] Iwata K 1983 *J. Chem. Phys.* **78** 2778
[93] Bird R B, Armstrong R C and Hassager O 1977 *Dynamics of Polymeric Liquids* (New York: Wiley) vol 1
[94] Everaers R and Kremer K 1994 *Comput. Phys. Commun.* **81** 19
[95] Allen M and Tildesley D 1987 *Computer Simulations of Liquids* (Oxford: Claredon)
[96] Ball R C and Edwards S F 1980 *Macromol.* **13** 748
[97] Everaers R 1994 *PhD thesis* University of Bonn (vol Jül-3040 of *Berichte des Forschungszentrums Jülich* (KFA Jülich, 1995)
[98] Koniaris K and Muthukumar M 1991 *Phys. Rev. Lett.* **66** 2211
[99] Barsky S J and Plischke M 1996 *Phys. Rev.* E **53** 871
[100] Barsky S J, Plischke M, Zhou Z and Joós B 1996 *Phys. Rev.* E **54** 5370

Video sequences

Video sequence 1
Preparation of random IPDNs [80]. Individual diamond networks are spanned across the simulation volume via periodic boundary conditions. We have chosen an average distance between connected cross-links of the order of the typical extension of corresponding chains in a melt. The network strands are modeled as bead-spring chains of uniform length. The extra beads, which serve as cross-linkers, are originally placed on the sites of a diamond lattice. Between them, we arrange random coil conformations of the network strands and randomize the initial conformation in MD runs for phantom chains. Since the density of a single diamond net decreases with the strand length, we superimpose several of these structures in the simulation box to reach melt density. The topology is conserved after building up the repulsive excluded volume interaction between the monomers. Different chains can no longer cut through each other and the random entanglements between meshes of the different networks become permanent.

Video sequence 2
While our main efforts were directed at measuring and understanding the significant entanglement contribution to the elastic modulus at small elongations, we also found that entanglements can be visualized by analysing the local stress distribution in strongly stretched networks [80]. The video compares regular and random IPDNs with $N = 12$. Particles which make large contributions to the virial expression for the stress tensor are shown with a larger diameter and marked in red. The apparent interruption of the chains is due to the representation in periodic boundary conditions. The stress localization in diamond networks is completely unexpected from the point of view of the classical theory, since all network strands are equivalent. The highly artificial regular IPDN mimic a situation where this equivalence is preserved for a conserved topology. When these networks are stretched, all strands contribute equally to the elastic response. Tensions are homogeneous throughout the whole system, and all strands are stretched to their full contour length at the maximal elongation. In random IPDN, on the other hand, completely stretched chains occur at much smaller elongations. A large part of the tension is localized on topologically shortest paths through the system. In particular, these paths are composed of strands as well as meshes with physical entanglements propagating the tension in the same manner as chemical cross-links. The way the chains fail and release entanglements is an artifact of our model. At too large stresses the connected beads at the contact points are driven so far apart that the chains can slip through each other. Since the energy threshold is of the order of $70k_{\mathrm{B}}T$ such events do not occur at small elongations.